The Supersonic Project: The Eccentricity and Rotational Support of SIGOs and DM GHOSts

Claire E. Williams[1,2], Smadar Naoz[1,2], William Lake[1,2], Yeou S. Chiou[1,2], Blakesley Burkhart[3,4],
Federico Marinacci[5], Mark Vogelsberger[6], Gen Chiaki[7], Yurina Nakazato[8], and Naoki Yoshida[8,9,10]

[1] Department of Physics and Astronomy, UCLA, Los Angeles, CA 90095, USA; clairewilliams@astro.ucla.edu
[2] Mani L. Bhaumik Institute for Theoretical Physics, Department of Physics and Astronomy, UCLA, Los Angeles, CA 90095, USA
[3] Department of Physics and Astronomy, Rutgers, The State University of New Jersey, 136 Frelinghuysen Rd, Piscataway, NJ 08854, USA
[4] Center for Computational Astrophysics, Flatiron Institute, 162 Fifth Avenue, New York, NY 10010, USA
[5] Department of Physics & Astronomy "Augusto Righi," University of Bologna, via Gobetti 93/2, I-40129 Bologna, Italy
[6] Department of Physics and Kavli Institute for Astrophysics and Space Research, Massachusetts Institute of Technology, Cambridge, MA 02139, USA
[7] Astronomical Institute, Tohoku University, 6-3, Aramaki, Aoba-ku, Sendai, Miyagi 980-8578, Japan
[8] Department of Physics, The University of Tokyo, 7-3-1 Hongo, Bunkyo, Tokyo 113-0033, Japan
[9] Kavli Institute for the Physics and Mathematics of the Universe (WPI), UT Institute for Advanced Study, The University of Tokyo, Kashiwa, Chiba 277-8583, Japan
[10] Research Center for the Early Universe, School of Science, The University of Tokyo, 7-3-1 Hongo, Bunkyo, Tokyo 113-0033, Japan
Received 2022 November 8; revised 2023 January 30; accepted 2023 January 31; published 2023 March 1

Abstract

A supersonic relative velocity between dark matter (DM) and baryons (the stream velocity) at the time of recombination induces the formation of low-mass objects with anomalous properties in the early universe. We widen the scope of the "Supersonic Project" paper series to include objects we term Dark Matter + Gas Halos Offset by Streaming (DM GHOSts)—diffuse, DM-enriched structures formed because of a physical offset between the centers of mass of DM and baryonic overdensities. We present an updated numerical investigation of DM GHOSts and Supersonically Induced Gas Objects (SIGOs), including the effects of molecular cooling, in high-resolution hydrodynamic simulations using the AREPO code. Supplemented by an analytical understanding of their ellipsoidal gravitational potentials, we study the population-level properties of these objects, characterizing their morphology, spin, radial mass, and velocity distributions in comparison to classical structures in non-streaming regions. The stream velocity causes deviations from sphericity in both the gas and DM components and lends greater rotational support to the gas. Low-mass ($\lesssim 10^{5.5} M_\odot$) objects in regions of streaming demonstrate core-like rotation and mass profiles. Anomalies in the rotation and morphology of DM GHOSts could represent an early universe analog to observed ultra-faint dwarf galaxies with variations in DM content and unusual rotation curves.

Unified Astronomy Thesaurus concepts: Galaxy formation (595); Dwarf galaxies (416); Galaxy rotation curves (619); High-redshift galaxies (734)

1. Introduction

According to the standard ΛCDM (cosmological constant + cold dark matter) model of structure formation, small overdensities seeded by quantum fluctuations in the homogeneous matter fields of the early universe grew through gravitational collapse into structures. Prior to recombination ($z \sim 1100$), overdensities of baryonic matter were prevented from growing by the strong coupling between the baryonic and photonic fields. Dark matter (DM) overdensities, however, were free to collapse. By the time of recombination, when baryons decoupled from radiation, DM overdensities had grown to five orders of magnitude larger than the baryonic overdensities (e.g., Naoz & Barkana 2005). Once decoupled, baryons collapsed into the significantly larger DM potential wells, resulting in the formation of structures with a central baryon component inside a larger DM halo (e.g., Wechsler & Tinker 2018).

This ΛCDM picture of structure formation is very successful on large scales (e.g., Springel 2005; Vogelsberger et al. 2014a, 2014b; Schaye et al. 2015; Vogelsberger et al. 2020). Uncertainties and tensions remain, however, especially on the

scales of faint dwarf galaxies (e.g., Bullock & Boylan-Kolchin 2017; Simon 2019; Perivolaropoulos & Skara 2022). From uncertainties such as the core-cusp challenge (e.g., Flores & Primack 1994; Moore 1994) to serious tensions such as the observed diversity of rotation curves compared to simulations (e.g., Oman et al. 2015, 2019), challenges to ΛCDM at low masses include not only tensions with observations (e.g., Webb et al. 2022) but also discrepancies between different state-of-the-art cosmological simulations (see Sales et al. 2022 for a review). The ultra-faint dwarf regime is thus expected to be one of the most sensitive probes of models and simulations of structure formation that succeed at the scales of Milky Way-like galaxies and larger mass dwarf galaxies. A precise description of the morphologies, dynamical histories, and star formation histories of ultra-faint galaxies under ΛCDM (and other models) will be central to resolving these tensions.

In an effort to refine the physical understanding of ΛCDM, Tseliakhovich & Hirata (2010) pointed out that previous work neglected the highly supersonic relative velocity ($v_{\rm bc}$) between DM and baryonic overdensities stemming from their five orders of magnitude difference in density. At recombination, the rms value of the relative velocity ($\sigma_{\rm vbc}$) was 30 km s^{-1}, five times the speed of sound of the baryons at the time. This velocity has important consequences for structure formation at small scales in the early universe. It is coherent over a few megaparsecs (Tseliakhovich & Hirata 2010), and on those scales it can be

modeled as a stream velocity of a single value. Recently, Uysal & Hartwig (2023) provided an observational estimate of the local value of $v_{bc} = 1.75^{+0.13}_{-0.28}\sigma_{vbc}$, suggesting that this effect was present during the formation of the Milky Way.

Subsequent works further explored the early universe implications of structure formation in the presence of the stream velocity. For example, the stream velocity was shown to delay the formation of Population III stars (e.g., Greif et al. 2011; Stacy et al. 2011; Schauer et al. 2017a) with impacts on reionization and the 21 cm signal (e.g., McQuinn & O'Leary 2012; Visbal et al. 2012; Muñoz 2019; Cain et al. 2020; Park et al. 2021; Long et al. 2022). It also suppresses halo abundance and generates "empty" halos with low gas content (e.g., Naoz et al. 2012; Asaba et al. 2016), generating large-scale inhomogeneities of galaxies (e.g., Fialkov et al. 2012) and affecting the minimum halo mass that holds most of its baryons (e.g., Naoz et al. 2013). Furthermore, in regions with a large relative velocity, gas accretion onto star-forming dwarf halos is affected—the gas falls downwind of halos, and has very low densities (e.g., O'Leary & McQuinn 2012). The stream velocity was shown to be responsible for reducing the number of low-mass, luminous satellite galaxies expected in ΛCDM, somewhat resolving an existing tension with observations at the time (e.g., Bovy & Dvorkin 2013). Low-mass galaxies in the stream velocity also have colder, more compact radial profiles (e.g., Richardson et al. 2013). Beyond galaxies, the stream velocity was suggested to enhance massive black hole formation (e.g., Tanaka et al. 2013; Latif et al. 2014; Tanaka & Li 2014; Schauer et al. 2017b; Hirano et al. 2017). In addition, the stream velocity produces supersonic turbulence, which can assist with the generation of early magnetic fields in the universe (Naoz & Narayan 2013).

Intriguingly, the stream velocity effect is also expected to induce the formation of objects with anomalous properties in patches of the universe with nonzero values of v_{bc}. Naoz & Narayan (2014) showed that the stream velocity introduces a phase shift between DM and baryon overdensities, which translates to a physical separation between the two components. Two interesting classes of objects arise from this effect that differ from classical ΛCDM objects at the same scales. First, for objects at a range of low masses ($\lesssim$few $\times 10^6\,M_\odot$), the spatial offset is so large that the baryonic component collapses outside the virial radius of its parent DM halo entirely, potentially surviving as a DM-deficient bound object. Naoz & Narayan (2014) proposed that these Supersonically Induced Gas Objects (SIGOs) may be the progenitors of globular clusters (e.g., Naoz & Narayan 2014; Popa et al. 2016; Chiou et al. 2018, 2019, 2021; Lake et al. 2021, 2023; Nakazato et al. 2022).

Second, for a range of slightly higher-mass objects ($\lesssim 10^8$ $M_\odot$), the spatial offset is such that the centers of mass of the baryonic component and the parent DM halo are offset, but the majority of the gas remains inside the DM virial radius (Naoz & Narayan 2014). We term these objects Dark Matter + Gas Halos Offset by Streaming (DM GHOSts). These structures consist of both a DM and gas component, unlike SIGOs, which are almost entirely gas. Compared to their classical ΛCDM analogs, DM GHOSts are enriched in DM and highly diffuse, because the stream velocity advects a portion of their gas component out of the halo. Naoz & Narayan (2014) suggested that these objects may be the progenitors of ultra-faint or dark-satellite galaxies.

The Supersonic Project was introduced to investigate supersonic stream velocity-induced objects and their ties to observed structures. Previous studies focused on the formation and evolution of SIGOs (e.g., Popa et al. 2016; Chiou et al. 2018, 2019, 2021; Lake et al. 2021, 2023; Nakazato et al. 2022). These simulations attempted to confirm the existence of SIGOs and investigate their connection to globular clusters using only adiabatic and sometimes atomic cooling. All except Schauer et al. (2021), Nakazato et al. (2022), and Lake et al. (2023) neglected the effects of molecular hydrogen cooling. Popa et al. (2016) and Chiou et al. (2019) placed early constraints on the rotational properties of SIGOs, showing that they are highly elongated structures with seemingly greater rotational support than both DM GHOSts and "classical" analogs–objects of the same mass in regions without streaming. Chiou et al. (2018, 2021) and Lake et al. (2023) focused on the potential for SIGOs to be sites of star formation. In a semi-analytic study, Chiou et al. (2019) found that SIGOs occupy a similar part of magnitude–radius space today as the population of observed globular clusters (e.g., McConnachie 2012). Lake et al. (2021) extrapolated the large-scale variation of SIGO abundances across the sky, predicting anisotropies in the distribution of gas-rich objects at low masses that could be observed by the James Webb Space Telescope (JWST) and binary black hole gravitational-wave sources detectable by gravitational-wave detectors.

Several recent studies indicate that molecular cooling may play an important role in the evolution of SIGOs and other objects in the stream velocity. Glover (2013) and Schauer et al. (2021) indicate that molecular cooling affects the abundance of gas objects in the early universe, and Nakazato et al. (2022) found that SIGOs became more filamentary in their molecular cooling simulations. Lake et al. (2023) studied the collapse of SIGOs in the context of molecular cooling, drawing an analogy to giant molecular clouds, and found that SIGOs should form stars outside DM halos. Studies have neither investigated DM GHOSts in detail nor constrained the rotational and morphological properties of the supersonically induced objects with molecular cooling.

Here, we present an updated analysis of the morphology, rotation, rotational curves, and mass distribution of both SIGOs and DM GHOSts using molecular hydrogen cooling numerical simulations supplemented by an analytical perspective. We characterize the population-level properties of these elongated objects in the context of ellipsoid potentials, and quantify their total angular momentum and rotational support. We find that the DM component deviates from a spherical configuration in the presence of the stream velocity. We also present the first rotation curves for these objects, finding a bifurcation in rotation curve shape according to mass. This may serve as an early universe analog to the rotational curve diversity observed in dwarf galaxies (e.g., Sales et al. 2022).

The paper is organized as follows: Section 2 describes the numerical simulations used in the study and the classification criteria for SIGOs and DM GHOSts. Section 3.1 is devoted to the analytical and numerical results of the study. In Section 3.1.1, we present the analytical ellipsoid potentials used to understand supersonically induced objects, and we show the population-level morphological properties of SIGOs and DM GHOSts from our simulations in Section 3.1.2. In Section 3.2, we discuss the rotational support and angular momentum of these objects. In Section 3.3, we present density

profiles and rotation curves of DM GHOSts. A summary and discussion of the results is given in Section 4. The appendices explain the choice of cutoff gas fraction used to define a SIGO (Appendix A), a full derivation of the potential and total mass from Section 3.1.1 (Appendix B), and supplemental morphological data, including comparisons to Navarro–Frenk–White (NFW) profiles (Appendix C).

In this study we assume a ΛCDM cosmology, with $\Omega_\Lambda = 0.73$, $\Omega_m = 0.27$, $\Omega_b = 0.044$, $\sigma_8 = 1.7$, and $h = 0.71$. The value of $\sigma_8 = 1.7$ adopted here is discussed in Section 2.3.

2. Numerical Setup

In a similar manner to previous studies by the Supersonic Project (e.g., Chiou et al. 2018, 2019, 2021), we perform hydrodynamical simulations using the AREPO code (Springel 2010). AREPO is a moving-mesh code that allows for high-resolution studies of structure formation with an accurate picture of the stream velocity up to $z \sim 20$.

2.1. Simulation and Initial Conditions

We use a modified CMBFAST code (Seljak & Zaldarriaga 1996), as presented in Popa et al. (2016), to include the first-order correction of scale-dependent temperature fluctuations on the initial conditions and their transfer functions, following Naoz & Barkana (2005). This is necessary as the corrections determine the gas fraction in halos at higher redshift (e.g., Naoz et al. 2009, 2011, 2013).

Tseliakhovich & Hirata (2010) showed that the supersonic relative velocity is coherent on scales of order a few megaparsecs, so following Popa et al. (2016), we choose a box size of two comoving megaparsecs, such that the relative velocity can be modeled as a stream velocity. Evolution of the stream velocity, a second-order correction (Tseliakhovich & Hirata 2010), is also included in the transfer functions. The simulations begin at $z = 200$, when a 2σ fluctuation in the stream velocity corresponds to 11.8 km s^{-1}. The stream velocity is thus implemented as a boost of 11.8 km s^{-1} to all baryon particles in the $+x$-direction. The box of two comoving megaparsecs contains 512^3 DM particles with a mass resolution of $m_{DM} = 1.9 \times 10^3 \, M_\odot$ and 512^3 Voronoi mesh cells representing the gas component, with a mass resolution of $m_{gas} = 360 \, M_\odot$. Our results are presented at the end of the simulations, $z = 20$.

To investigate the effect of the stream velocity, we perform two runs without the stream velocity (i.e., runs in a region of space with a $0\sigma_{v_{bc}}$ fluctuation in the velocity field) and two runs with a value of $v_{bc} = 2\sigma_{v_{bc}}$. For each set of two runs (with and without the stream velocity), we include molecular (H$_2$) cooling in one and only adiabatic cooling in the other. The inclusion of molecular cooling is described in Section 2.2 below. Our chosen value of $v_{bc} = 2\sigma_{v_{bc}}$ is similar to the local observed value $v_{bc} = 1.75^{+0.13}_{-0.28}\sigma_{vbc}$ (Uysal & Hartwig 2023).

2.2. Molecular Cooling

To understand the effect of molecular cooling, we perform two runs for each value of the stream velocity ($0\sigma_{v_{bc}}$ and $2\sigma_{v_{bc}}$), one with adiabatic cooling only and one with molecular cooling included. We denote the H$_2$ cooling runs with "H2." The 0vH2 and 2vH2 runs were also used in Lake et al. (2023). A summary of the runs in this work is given in Table 1.

Table 1
Simulation Parameters

Run	v_{bc}	H$_2$ Cooling
0v	0	No
2v	$2\sigma_{v_{bc}}$	No
0vH2	0	Yes
2vH2	$2\sigma_{v_{bc}}$	Yes

As in Nakazato et al. (2022) and Lake et al. (2023), we explicitly account for nonequilibrium chemical reactions and radiative cooling in the gas, using GRACKLE, a chemistry and cooling library (Smith et al. 2017; Chiaki & Wise 2019). The 0vH2 and 2vH2 runs include H$_2$ and HD molecular cooling. The radiative cooling rate of the former includes both rotational and vibrational transitions (Chiaki & Wise 2019). Chemistry for the following 15 primordial species is included in the H2 runs: e$^-$, H, H$^+$, He, He$^+$, He^{++}, H$^-$, H$_2$, H$_2^+$, D, D$^+$, HD, HeH$^+$, D$^-$, and HD$^+$. We do not include star formation.

2.3. Object Classification

We are interested in gas-rich structures, including SIGOs, which have somewhat low statistical power in these small box simulations. Thus, following Popa et al. (2016), Chiou et al. (2018), Chiaki & Wise (2019), Chiou et al. (2021), Lake et al. (2021, 2023), and Nakazato et al. (2022) we choose $\sigma_8 = 1.7$, which will increase the statistical power. This represents a region of the universe where structure forms early, such as in the Virgo cluster (e.g., Naoz & Barkana 2007). Because σ_8 produces a large statistical power, we increase the number of gas objects in the simulation without affecting the cosmology, and these results can then be scaled to other regions accordingly (e.g., Naoz et al. 2013; Park et al. 2020).

To identify structures, we search for two object classes using a friends-of-friends (FOF) algorithm (see e.g., Popa et al. 2016; Chiou et al. 2018).

1. DM-primary/Gas-secondary (DM/G) objects are found using the FOF algorithm on DM particles first. Gas cells in the same object are associated with the DM groups at a secondary stage. We require DM/G objects to have at least 300 DM particles, to avoid numerical artifacts.
2. Gas-primary (GP) objects are found using the FOF algorithm only on gas cells. This allows us to find objects such as SIGOs in the simulation that have little or no DM component. We require GP objects to have at least 100 gas cells, again in order to avoid nonphysical numerical effects.

The choice to cut off the DM/G and GP objects at 300 particles and 100 cells, respectively, gives us a minimum structure mass resolution of $5.7 \times 10^5 \, M_\odot$ for DM/G and $3.6 \times 10^4 \, M_\odot$ for GP objects.

Popa et al. (2016) and Chiou et al. (2018) found that GP objects are often filamentary in nature, and thus a spherical fitting algorithm is not an optimal choice, as it does not reflect the actual morphology of these structures. We therefore employ the same fitting algorithm of these works, which is based on a triaxial ellipsoid fit. We keep the axis ratio of a triaxial ellipsoid with N_0 gas particles and maximum radius $R_{max,0}$ around the GP object constant and shrink it in increments of 0.5 percent until the condition $R_{max,n}/R_{max,0} > N_n/N_0$ is met, or until
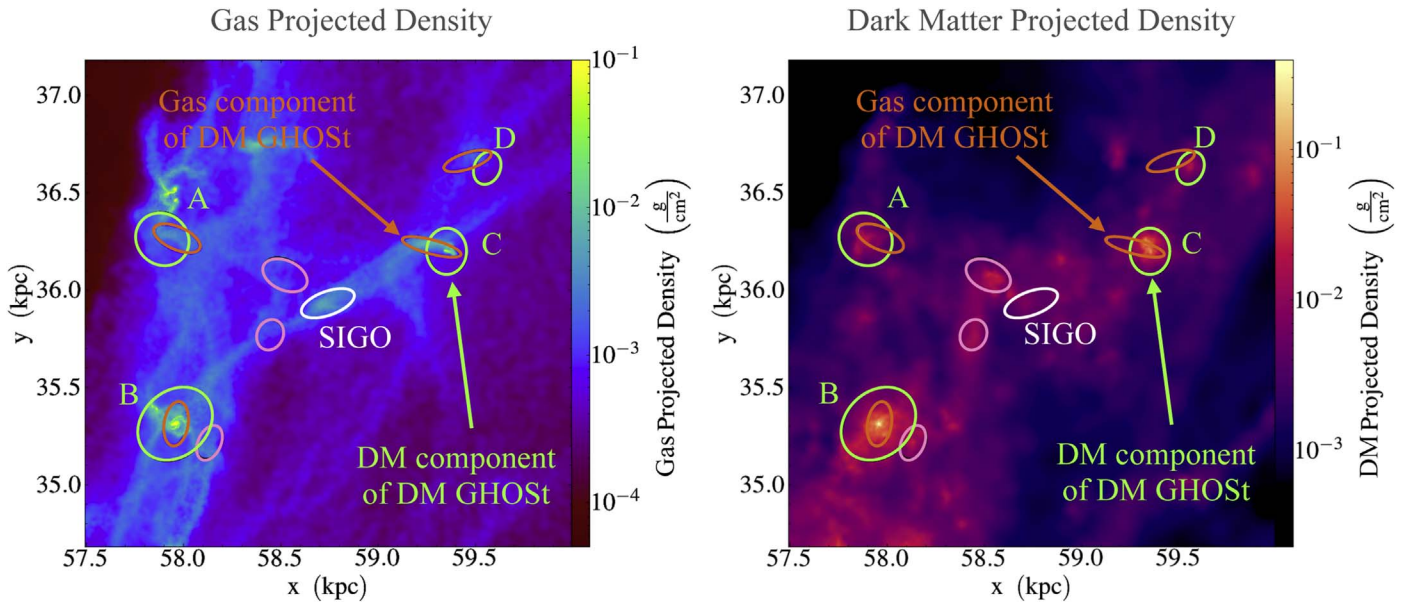
Figure 1. Projected gas (left) and DM (right) density around several DM GHOSts and a SIGO in a physical region 5 kpc on a side. The SIGO is bounded by the white ellipse, located in a region relatively devoid of DM, and contains no DM component. It is embedded in a stream of gas. The DM GHOSts (A, B, C, and D) each contain a gaseous and a DM component. The gas components of the DM GHOSts are shown in orange, whereas the DM components of the DM GHOSts are shown in green. The DM components are not entirely spherical. The ellipses enclosing the DM components are those found by the method described in Section 2.3 and do not correspond to the DM virial radius of the object, used in the criterion to determine whether an object is a SIGO. The centers of mass of the gas components of A, C, and D are offset from the centers of mass of the DM component, whereas B has had time for the gas component to fall back into the center of the DM potential. Several DM halos with no associated gas components also lie in this region–depicted in pink. One of these may be the "parent" halo of the SIGO.

$N_n/N_0 < 0.8$, where $R_{\mathrm{max,n}}$ and N_n are the maximum ellipsoid radius and number of gas particles of the nth iteration.

The GP FOF algorithm is performed to identify SIGOs, gas-rich objects that form outside the virial radius of the parent DM halos. However, many of the GP objects are located inside DM halos, being the gas component of the DM/G structures. These structures are also of interest to this study. In order to clarify the difference between structures formed via classical ΛCDM and these DM and gas structures formed in regions with the stream velocity, we term the DM/G objects in regions of streaming as DM GHOSts. In previous papers, these were referred to as "DM/G." Having formed offset from the center of mass of their parent DM halo, these structures display different morphological and dynamical properties than those that formed in regions of the universe with no relative velocity (i.e., a patch with a $0\sigma_{v_{\mathrm{bc}}}$ fluctuation), even though many are no longer offset by the redshifts considered here due to dynamical processes (such as the DM GHOSt labeled "B" in Figure 1.)

We follow the convention in Nakazato et al. (2022), where SIGOs are defined as GP objects which meet the following two conditions:

1. They are located outside the virial radius of their parent DM halo.
2. They contain a gas fraction,

$$f_g = \frac{M_g}{M_{\mathrm{DM}} + M_g} > 0.6, \qquad (1)$$

where M_g is the total mass of gas in the object and M_{DM} is the total mass of DM in the object.

Similar criteria were used in Popa et al. (2016), Chiou et al. (2018, 2019, 2021), and Lake et al. (2021). The gas fraction cutoff in those works was chosen rather arbitrarily to be 0.4. This value was implemented because those studies were

interested specifically in the gas-rich structures in connection with observed DM-deficient objects such as globular clusters. Our cutoff gas fraction of 0.6 is higher. Nakazato et al. (2022) found that choosing a smaller cutoff gas fraction in runs with molecular cooling leads to the identification of filamentary structures as SIGOs, such that without the stream velocity many SIGOs are misidentified. We find similar behavior in our molecular cooling run, and this choice of gas fraction is discussed further in Appendix A. GP objects in runs with stream velocity that do not meet the SIGO criteria above are classified as the baryonic component of DM GHOSts.

A DM GHOSt therefore contains two components: a DM component, identified by the DM/G FOF algorithm, and a gaseous component, identified by the GP FOF. For DM GHOSts, the GP FOF often identifies the gas structure within the DM-primary object. Figure 1 shows the projected density of DM (left) and gas (right) in a region of the simulation box with four DM GHOSts and a SIGO. The SIGO contains only a component identified by the GP FOF, which can be clearly seen in the plot of the gas density. The DM GHOSts are found in both particle FOF types and have two overlapping (but offset) components.

In Chiou et al. (2019) and subsequent papers, a spherical overdensity calculation was used to obtain the virial radius of the DM halos. However, in this study we sought to explore the morphology of the diffuse DM GHOSts and their DM component. Thus, we also perform an ellipsoid fit as described above to the DM/G objects to explore whether they deviate from a spherical morphology. So, as before, a triaxial ellipsoid with a fixed axis ratio is fit to the DM/G object, shrinking in 0.5% increments until the axis ratio is less than the ratio of the number of particles in the original object to the shrunken ellipsoid, or 20% of the particles are removed.

A table of the GP objects found using the FOF algorithm described here is presented in Table 2. The probability density

Table 2
Summary of the Number of GP Objects and Subclasses Found in the Four Runs
Used in This Study

Run	# GP	# SIGOs	# DM GHOSts
0v	2557	⋯	⋯
2v	759	25	734
0vH2	5823	⋯	⋯
2vH2	1406	69	1337

Note. Only objects containing over 100 gas particles are included. SIGOs and DM GHOSts do not exist in regions with 0 stream velocity, so they are not tabulated for the 0v and 0vH2 runs; but see Appendix A for an investigation of false identification of SIGOs in molecular cooling runs.

distributions in Section 3 are calculated from this set of objects, with a Gaussian kernel density function using a Scott bandwidth (Scott 2010).

3. Physical Properties and Analytical Description

In combination with an analytical understanding, this section describes the morphological and rotational properties of the population of numerically simulated structures from the four simulation runs described above.

3.1. Morphology

Historically, spherical overdensity calculations have been used to understand the gravitational potentials of the universe's first structures (see Barkana & Loeb 2001 for a review). However, both the stream velocity and molecular cooling were shown to induce gaseous filaments and elongate structures. For this reason, we introduce the eccentricity as a measure of an object's deviation from an idealized spherical configuration, and present an analytical potential for SIGOs and DM GHOSts in terms of their eccentricity. A full derivation of the potential and other relevant equations is given in Appendix B.

3.1.1. Analytical Ellipsoid Potential of SIGOs and DM GHOSts

In order to explore the role of the eccentricity in the gravitational potential analytically, we approximate SIGOs and DM GHOSts as prolate ellipsoids, with $R_{max} > R_{mid} \sim R_{min}$. We show in Section 3.1.2 that this approximation is consistent with the structures found in the simulation.

In cylindrical coordinates (R, z), the gravitational potential (Φ) of a prolate ellipsoid can be written as,

$$\Phi(x) = -2^{3/2} \frac{4\pi G R_{max}^4 \, \rho(R_{max}^2) \cos^{-1}(\sqrt{1-e^2})}{e\sqrt{1 + (1-e^2)\left(\frac{R^2}{R_{min}^2} + \frac{z^2}{R_{max}^2}\right)}}, \quad (2)$$

where G is the gravitational constant, R_{max} is half the length of the maximum axis of the ellipsoid, R_{min} is half the length of the minimum axis of the ellipsoid (see Figure 2), $\rho(R_{max}^2)$ is the density at R_{max}, and e is the eccentricity. See Appendix B for a derivation of Equation (2). The eccentricity is a measure of the ellipsoid elongation, defined (following the convention used in
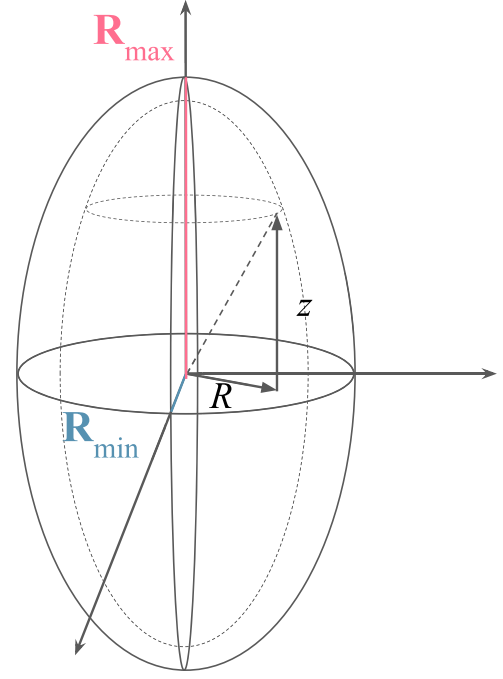

Figure 2. Choice of coordinates adopted in this work. The ellipsoids are arranged such that the primary axes of the ellipsoid are aligned along the Cartesian coordinate directions, with R_{max}, the polar radius of a prolate spheroid, along the z-axis. In the prolate approximation, $R_{min} \sim R_{max}$. Cylindrical coordinates are used in Section 3.1.1 as the natural choice for prolate ellipsoid potentials.

Binney & Tremaine 2008) as,

$$e \equiv \sqrt{1 - \left(\frac{R_{min}}{R_{max}}\right)^2}. \quad (3)$$

This parameter resembles the 2D ellipse eccentricity, and varies from 0 (spherical) to 1 (radial). Previous works by the Supersonic Project (Chiou et al. 2018) used the prolateness factor (ξ) to characterize the shape of GP objects,

$$\xi = \frac{R_{max}}{R_{min}}. \quad (4)$$

The relation between the eccentricity and the prolateness factor is,

$$e = \sqrt{1 - \xi^{-2}}. \quad (5)$$

In deriving the potential in Equation (2), we have assumed a prolate spheroidal density profile given by,

$$\rho(m^2) = \rho_0 \left[1 + \left(\frac{m}{R_{max}}\right)^2\right]^{-\frac{3}{2}}, \quad (6)$$

where m is defined in cylindrical coordinates as,

$$m^2 \equiv \frac{R^2}{1 - e^2} + z^2, \quad (7)$$

(Binney & Tremaine 2008). Note that $0 \leqslant m \leqslant R_{max}$. In the above formalism, we scale the density such that $\rho_0 = 2^{3/2}\rho(R_{max})$.

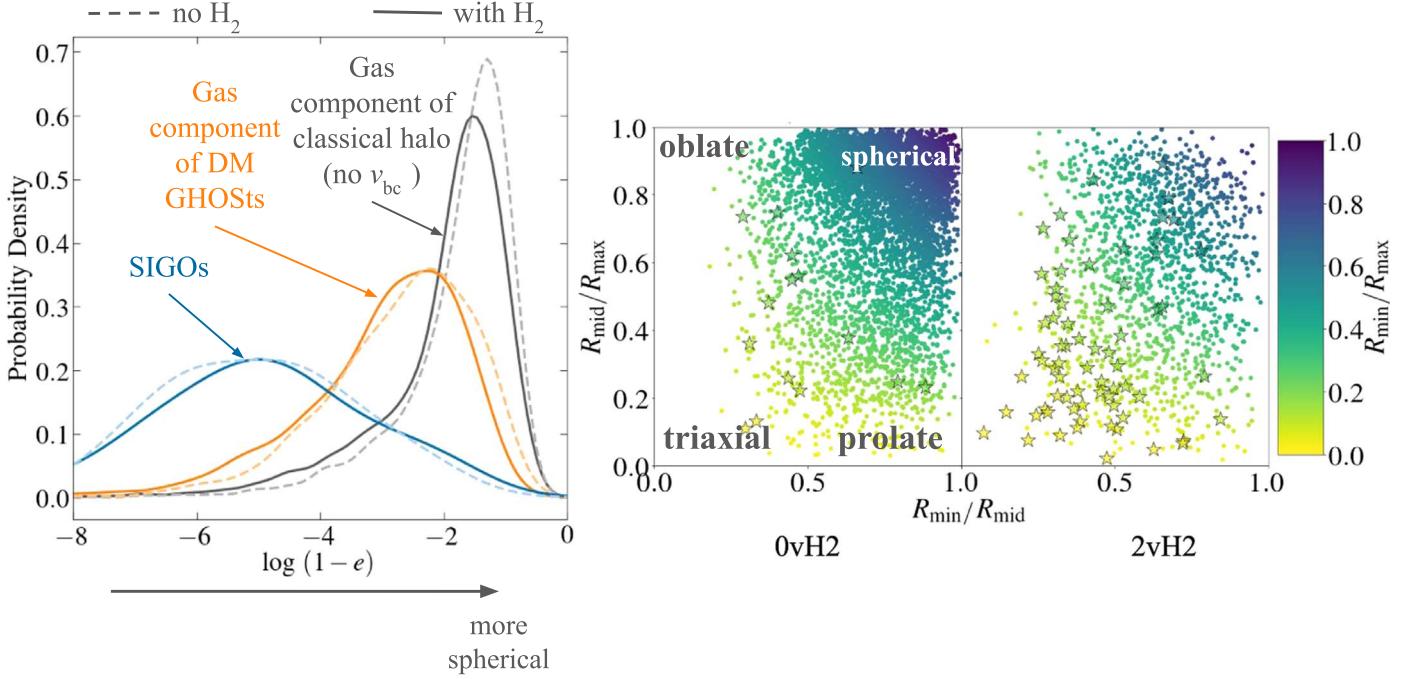From here, we find the dependence of the total mass on eccentricity. Once again, a complete derivation can be found in

Figure 3. Left: probability density distribution of $\log(1 - e)$, where e is the eccentricity (Equation (3)), for GP objects. The distributions are separated into the object classes listed in Table 2 and calculated using a Gaussian kernel density. The orange distributions show the gas component of DM GHOSts, the gray distributions show the gas component of classical halos (without v_{bc}), and the blue distributions show SIGOs. The darker lines denote runs with H_2 cooling, while the lighter dashed lines denote no cooling. Right: scatterplot of R_{mid}/R_{max} vs. R_{min}/R_{mid} for GP objects in the H_2 cooling runs. The color bar shows R_{min}/R_{max}. The left column has no stream velocity and the right column is from the $v_{bc} = 2\sigma_{v_{bc}}$ runs (see Table 2). Stars represent SIGOs, as defined in Section 2.3. In order to make a comparison between the cases with and without the stream velocity, we make an arbitrary cutoff that all three axis ratios must be $\geqslant 0.9$. For the no stream velocity case, we find 40 objects (0.6%) that are spherical by this definition in the 0vH2 run and 11 objects (0.4%) that are spherical in the 0v run. With the stream velocity, we find 0 objects in 2vH2 and 1 object in 2v that meet the criterion.

Table 3
Mean Values of the Selected Parameters Presented in This Work for the Four Runs

Run	0v	2v			0vH2	2vH2		
Objects	All	SIGOs	DM GHOSts	All	All	SIGOs	DM GHOSts	All
Gas Eccentricity	7.75E-01	9.82E-01	8.88E-01	8.92E-01	8.06E-01	9.77E-01	9.11E-01	9.15E-01
DM Eccentricity	8.22E-01	X	8.19E-01	X	7.69E-01	X	8.12E-01	X
Gas Spin	9.12E-02	1.21E-01	1.53E-01	1.52E-01	6.44E-02	1.80E-01	1.26E-01	1.31E-01
DM spin	3.25E-01	X	2.33E+00	X	4.25E-01	X	1.29E+00	X
Total mass ($M_\odot$)	9.91E+05	3.61E+04	1.75E+06	1.69E+06	5.39E+05	1.98E+05	1.35E+06	1.29E+06
Gas Fraction	1.20E-01	8.26E-01	1.47E-01	1.72E-01	2.70E-01	7.72E-01	2.30E-01	2.60E-01

Note. For the 2v and 2vH2 runs, means are given also for the populations of SIGOs and DM GHOSts separately.

Appendix B. The total mass of the ellipsoid is found by integrating over a set of similar ellipsoids from the center to the outer edge of the object (i.e., $m = 0$ to $m = R_{max}$). Thus, for an object with density given by Equation (6), we find the total mass of the object M,

$$M = 4\pi (2^{3/2} \rho_{max})(1 - e^2) R_{max}^3 \left(\sinh^{-1}(1) - \frac{1}{\sqrt{2}} \right)$$

$$\approx 6.19 \rho_{max}(1 - e^2) R_{max}^3. \qquad (8)$$

Below we use the eccentricity parameter to estimate the prolateness of the SIGOs and DM GHOSts. We also compare the eccentricity inferred by the analytical ellipsoid potential (Equation (2)) for an average object with our simulated objects' eccentricities versus the mass enclosed within the ellipsoid bounding each object, finding agreement between the analytic and numeric results for eccentric objects.

3.1.2. Morphologies of the Numerically Simulated Objects

In the previous section we assumed a prolate relation between the ellipsoid axes ($R_{max} > R_{mid} \sim R_{min}$). Interestingly, we find that both the gas component and the DM component of structures become prolate in the presence of the stream velocity as depicted in Figure 3.

The left panel of Figure 3 shows probability density distributions for the eccentricity of GP objects in all four runs. The gas components of classical halos (i.e., no stream velocity), SIGOs, and DM GHOSts comprise three distinct populations in eccentricity. The stream velocity induces elongation of objects, with objects in the 0v and 0vH2 runs being the most spherical. Among the supersonically induced objects, SIGOs are more elongated and prolate than DM GHOSts. The average SIGO eccentricity of 0.977 corresponds to an object whose R_{min} is only around 20% of its R_{max}, whereas for a classical object with molecular cooling the average ratio is around 60% (see Table 3
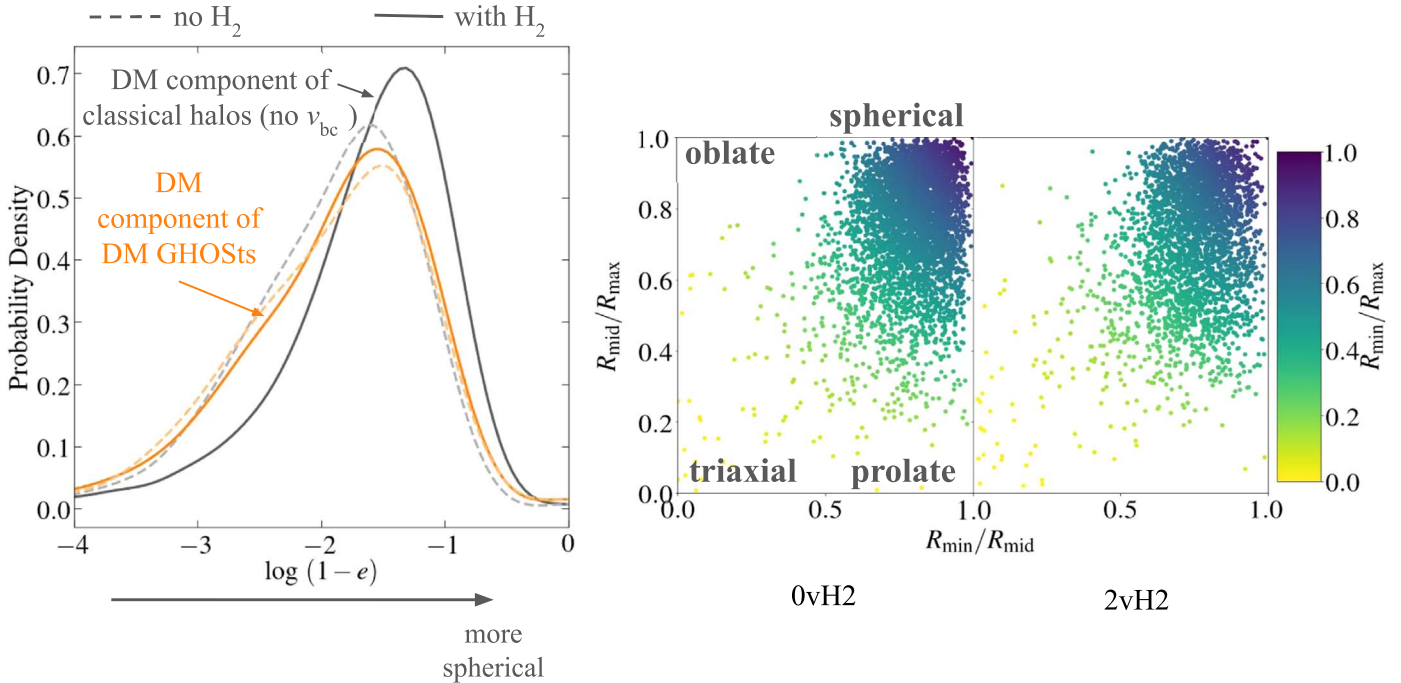
6

Figure 4. Left: probability density distribution of $\log(1 - e)$ of DM-primary objects, where e is the eccentricity (see Equation (3)). The orange distributions show the DM component of DM GHOSts and the gray distributions show the DM component of classical halos without v_{bc}. SIGOs, which have little to no DM component, are not plotted. The darker lines denote runs with H_2 cooling, while the lighter dashed lines denote no cooling. Right: scatterplot of R_{mid}/R_{max} vs. R_{min}/R_{mid} for DM-primary (DM/G) objects. The color bar shows R_{min}/R_{max}. The left column has no stream velocity and the right column is from the $v_{bc} = 2\sigma_{v_{bc}}$ runs (see Table 2). SIGOs are not included because they have no DM component. These results imply that the DM component for the majority of objects is nonspherical, and the stream velocity induces further elongation.

for the mean values of the morphological parameters). The stream velocity effect dominates runs with and without molecular cooling, but in the no stream velocity case, molecular cooling also slightly elongates the gas component.

The stream velocity also affects the shape of the DM component of DM GHOSts, resulting in elongated DM structures. The left panel of Figure 4 shows the distribution of eccentricities of the DM-primary objects in the 0v and 0vH2 runs and DM GHOSts with and without cooling. Including H_2 cooling, the DM component of DM GHOSts tends to be less spherical than the classical DM halos.

The eccentricity is only a measure of the difference between the minimum and maximum radii of the ellipsoid. Therefore, to justify the prolate approximation, we show the ratios of all three axes of the gas (Figure 3, right panel) and DM (Figure 4, right panel) components of the ellipsoids. The parameter space is divided into spherical, triaxial, oblate, and prolate objects. Even without a stream velocity, there is a range of morphologies among both the DM and gas components of the structures. The probability density distributions of all the ratios are given in Appendix C. As seen in the figures, the majority of the DM components are spherical in nature, and those that deviate from sphericity tend to be prolate.

For the gas components (top right panel in Figure 3), as expected, the majority of the gas component of the classical objects is spherical, with preference toward a prolate configuration. The stream velocity elongates objects into more extreme axis ratios. In fact, there are scarcely few truly spherical objects in the runs with the stream velocity. SIGOs, shown as stars in the figure, have not only the most extreme eccentricities overall, but also tend toward the triaxial region of the figure.

In Figure 5, we plot the eccentricity of the objects' gas component as a function of mass. We overlay the expected relation from Equation (8) for objects of average density and scale (solid line). Recall that this equation represents the relationship between the mass and the elongation for an ellipsoid potential. Thus, for the no stream velocity case, where the majority of the structures are spherical (i.e., $\log(1 - e^2) = 0$) most of the objects are concentrated at low eccentricity. However, more elongated objects in runs with the stream velocity follow the trend outlined by Equation (8). In particular, for the no cooling case, the plot shows a more elongated structure for smaller-mass systems. However, cooling, even in the presence of the stream velocity, tends to assist with collapse, thus resulting in a deviation compared to the analytical prediction. Note that in general, cooling still tends to create more elongated structures (this was also highlighted in Lake et al. 2021; Nakazato et al. 2022). In the bottom plot of Figure 5, we plot the same relation for the DM/G objects. Again, those that are more eccentric in nature follow the trend derived from the ellipsoid potential, while many halos, especially classical halos, are concentrated toward circularity.

3.2. The Spin Parameter

The angular momentum of galaxies has long been understood to be closely tied to their formation and evolution (e.g., Peebles 1969; Fall & Efstathiou 1980). In particular, the relationship between the angular momentum of the DM halo and the gas seems critical in shaping the final galactic morphology and spin parameter (e.g., Bullock et al. 2001; Maller & Dekel 2002; Danovich et al. 2015; Rodriguez-Gomez et al. 2017; Wechsler & Tinker 2018; Kurapati et al. 2021;
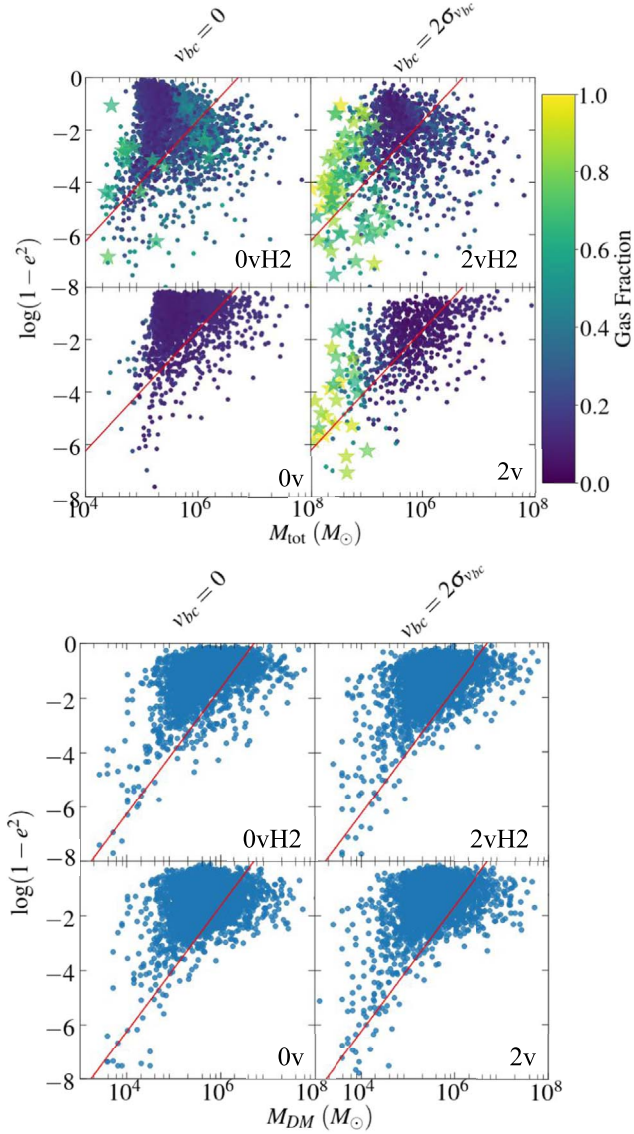
Figure 5. Top: scatterplot of $\log(1 - e^2)$ vs. $M_{\rm tot}$ for GP objects. SIGOs are denoted by stars. Bottom: scatterplot of $\log(1 - e^2)$ vs. $M_{\rm DM}$ for DM-primary (DM/G) objects (we include both the DM components of DM GHOSts and other DM halos in the box that have no associated GP component) In both plots, the top two panels show the H_2 cooling runs, and the bottom two panels show runs without cooling. The left column has no stream velocity and the right column is from the $v_{\rm bc} = 2\sigma_{v_{\rm bc}}$ runs. Stars represent SIGOs, as defined in Section 2.3. The color bar shows the gas fraction (Equation (1)). The red overplotted line is the expected relationship from Equation (8) for an example object with the average density and maximum radius of objects in the H_2 cooling runs ($\bar{\rho}_{R\,\rm max} = 1.8 \times 10^8 M_\odot\,{\rm kpc}^{-3}$ and $\bar{R}_{\rm max} = 0.134$ kpc).

Yang et al. 2023; Cadiou et al. 2022; Ebrahimian & Abolhasani 2022; Hegde et al. 2022; Rodriguez-Gomez et al. 2022; Rohr et al. 2022). DM halo spin in simulations follows a lognormal distribution (e.g., Bullock et al. 2001; Zjupa & Springel 2017), and the spin of the cold gas of galaxies seems to follow a similar distribution in observations and simulations (e.g., Danovich et al. 2015; Burkert et al. 2016). Models that conserve angular momentum suggest that the structure, size, and morphology of galaxies follow the mass and angular momentum of their host halos (e.g., Somerville et al. 2008; Guo et al. 2011; Benson 2012; Somerville & Davé 2015). Initially, simulations struggled to replicate observed properties of galaxies such as the large spin of the baryonic component

compared to the DM and the shape of the angular momentum of galaxies, but it was recognized that baryonic processes, including feedback, can explain the evolution of the angular momentum of the baryonic component (e.g., Maller & Dekel 2002; Teklu et al. 2015; Zjupa & Springel 2017; El-Badry et al. 2018; Rohr et al. 2022). Furthermore, some recent work (e.g., Sales et al. 2012; Danovich et al. 2015; Jiang et al. 2019) suggests that galaxies' spins are not correlated with the spins of their host halos at all, and observed scaling relations must be explained via other mechanisms. Persistent uncertainties in the relationship between angular momentum, morphology, and galaxy structure remain, particularly at low masses (e.g., Ebrahimian & Abolhasani 2022; Nguyen et al. 2023). Including $v_{\rm bc}$, which affects both the velocity and the configuration of the baryonic component, has already been shown to affect the spin at low masses (e.g., Chiou et al. 2018), and thus we continue with an investigation of the angular momentum of our sample of structures.

To quantify the rotation and angular momentum of objects, we follow the analytical formulation from Chiou et al. (2018). The total angular momentum, denoted by the spin vector ($J_{\rm sp}$) of a set of N particles each of mass m_i is,

$$J_{\rm sp} = \sum_{i=1}^{N} m_i r_i \times v_i, \qquad (9)$$

where r_i and v_i are the particles' position and velocity vectors, respectively, from the center of mass. For DM-primary objects, we estimate the angular momentum of the entire halo using the spin parameter (e.g., Peebles 1969) as defined in Bullock et al. (2000),

$$\lambda_{\rm DM} = \frac{J_{\rm sp}}{\sqrt{2}\,M_{200} v_{200} R_{200}}. \qquad (10)$$

Here M_{200} is the virial mass of the object, $v_{200} = \sqrt{GM_{200}/R}$ (Barkana & Loeb 2001), and $J_{\rm sp} = |J_{\rm sp}|$. Chiou et al. (2018) showed that the DM/G spin follows a lognormal distribution consistent with Bullock et al. (2001).

Following Chiou et al. (2018), in order to account for the more ellipsoidal nature of the gas component, we calculate the spin parameter for GP objects using,

$$\lambda_{\rm g} = \frac{J_{\rm g}}{6\sqrt{2}\,M_{\rm g} v_{\rm GP} R_{\rm max}}, \qquad (11)$$

where $M_{\rm g}$ is the total gas mass, $v_{\rm GP}$ is the circular velocity of the GP object at a distance $R_{\rm max}$, and $J_{\rm g}$ is calculated from Equation (9) for gas particles only.

Figure 6 shows the probability density distributions of the spin parameter of GP objects and DM-primary objects. The stream velocity induces a higher total spin for the gas component of all runs. However, for classical gas objects, molecular cooling serves to lower the total angular momentum by condensing gas inward, thus allowing for a smaller spin parameter. For classical objects, the DM components have a larger spin parameter magnitude overall: because DM constitutes most of the mass, it contributes most of the total angular momentum. On the other hand, the stream velocity boosts the gas spin for both SIGOs and the gas component of DM GHOSts, thus increasing the total angular momentum of the system despite H_2 cooling. SIGOs and DM GHOSts thus have
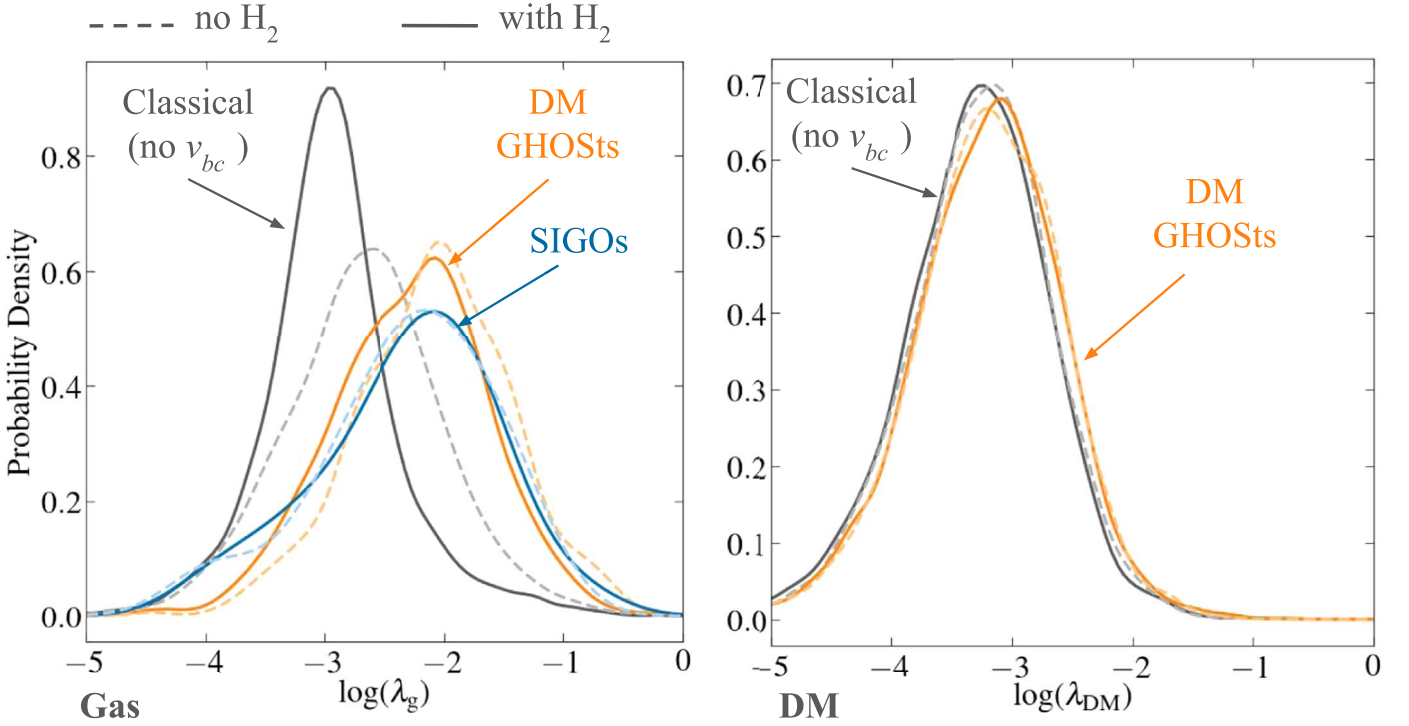
Figure 6. Probability density distributions of λ_g (left) and λ_{DM} (right). These are calculated via Equations (11) and (9), respectively. The distributions are separated into the object classes listed in Table 2 and calculated using a Gaussian kernel density. The orange distributions include the gas component of DM GHOSts, the gray distributions show the gas component of classical halos without v_{bc}, and the blue distributions show SIGOs. We do not include λ_{DM} for SIGOs since they are dominated by gas and the DM does not contribute significantly to the angular momentum of the system. The darker lines denote runs with H_2 cooling, while the lighter dashed lines denote no cooling.
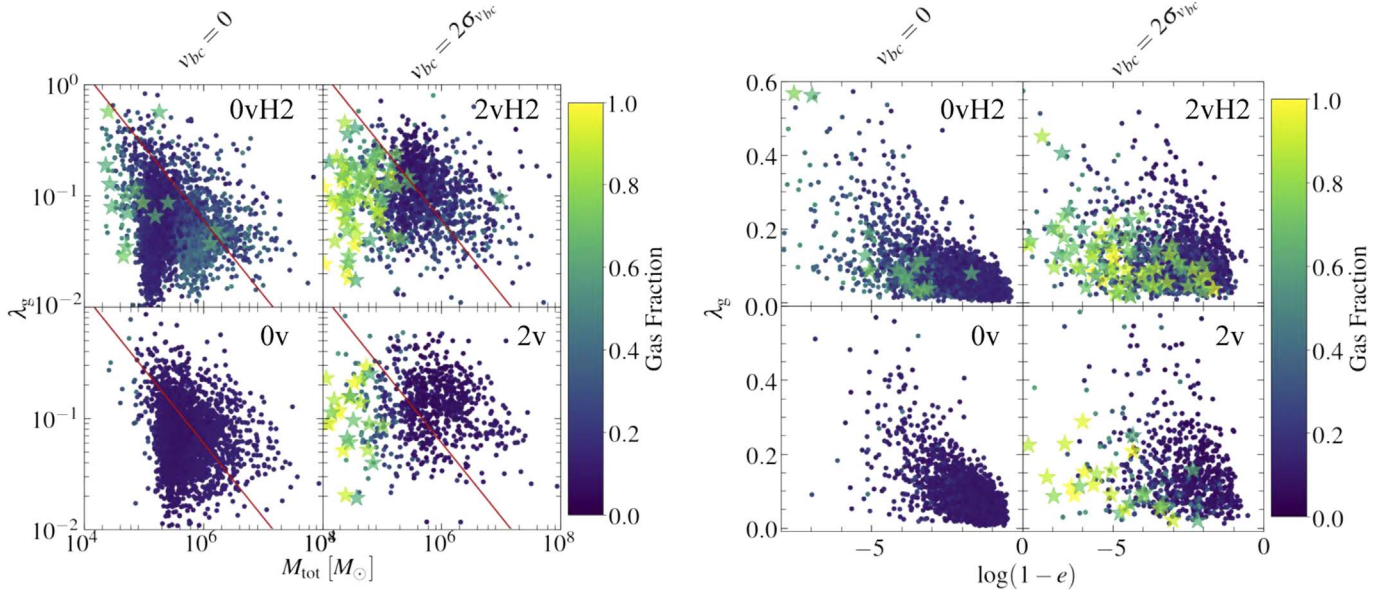
Figure 7. Scatterplot λ_g vs. the DM mass (M_{tot}) (left) and λ_g vs. $\log(1 - e)$ (right) of GP objects. The top row includes H_2 cooling. The left column denotes the runs without the inclusion of the stream velocity, and the right column contains runs with the stream velocity. A line corresponding to $\lambda_g \sim M^{-2/3}$ is overplotted in red on the left-hand side. This is the expected relation from Equation (11). The vertical cutoff at low masses is due to our resolution limit of 300 particles minimum (corresponding to a mass of $5.7 \times 10^5 \, M_\odot$), while at high mass we are limited by Poisson fluctuations of small number statistics at this high redshift and small box size.

gas spin parameters an order of magnitude larger than the no stream velocity gas (see Table 3).

In Figure 7, we plot the spin parameter against the total mass (left) and eccentricity (right) of the objects. More eccentric objects tend to have higher spins in all runs. The vector sum in

the definition of $\boldsymbol{J}_{sp}$ (Equation (9)) means that this parameter encodes not only the magnitude of the total angular momentum but also the alignment of the particles' rotations. Thus, the trend on the right of Figure 7 is consistent with spherical configurations corresponding to an isotropic distribution of the

particles' orbits. Further, it is consistent with prolate systems having a preferred directionality to the angular momentum or an ordered distribution of particle orbits.

Furthermore, the spins of the objects in the no stream velocity case roughly follow a $\lambda \sim M^{-2/3}$ slope; see the bottom left panel in Figure 7. This relation is expected from Equation (10) for mostly circular orbits. However, the trend dissipates in the presence of the stream velocity and cooling, where the objects deviate from spherical symmetry and the combined effects introduce a preferred directionality for the angular momentum, almost regardless of the mass. We attribute this to the turbulent and filamentary nature of these structures in the presence of the stream velocity and molecular cooling (e.g., Lake et al. 2023; Nakazato et al. 2022). Note that the cutoff in the low-mass regime is due to our resolution limit of 300 particles minimum (corresponding to a mass of $5.7 \times 10^5 \, M_\odot$), while at the high-mass regime we are limited by Poisson fluctuations of small number statistics at this high redshift and small box size.

The question of whether these larger spin parameters imply greater overall angular momentum or more ordered rotation leads us to an investigation the connection between the morphologies of the objects and their rotational support. An investigation of the ellipsoids' alignments with respect to the stream velocity direction revealed that SIGOs are not always aligned with R_{max} in the direction of the stream velocity. More frequently, they are embedded in a stream of gas that is infalling toward a larger DM halo (see Figure 1, for example), and their longest axis aligns with this stream of gas. Thus, to check how ordered these objects' rotations are, we test whether the rotation axis is aligned with any of the three primary ellipsoid axes.

To describe the directionality of the angular momentum we utilize spherical coordinate notation. With the maximum radius aligned with the z-axis and the minimum radius aligned with the x-axis, we calculate the spherical θ and ϕ components of the spin vector of both the DM and gas of the objects. Figure 8 shows an illustration of the orientation of the ellipsoid with respect to the spin vector.

Figure 9 shows distributions of the misalignment between the primary ellipsoid axes and the spin vector for both the gas component (top row) and the DM component (middle row). As depicted, the classical halos (both for the DM and gas components) are preferentially spinning in alignment with their minimum axis, and do not show a preference with respect to their maximum axis. These classical halos were the most oblate group overall, thus the lack of preference for alignment with the maximum axis could be due to the fact that for an oblate spheroid, $R_{\mathrm{max}} \sim R_{\mathrm{mid}}$. In other words, they are consistent with puffy disks. The bottom row of Figure 9 shows a cartoon depiction of the range of preferred rotation of the classical objects here.

DM GHOSts, to a lesser degree, are rotating in alignment with their minimum axis, but they also show a preference toward the maximum axis. This "spinning top" type of behavior seems to be consistent when considering their formation (see Figure 3 in Lake et al. 2023). The gas component of DM GHOSts (similar to classical objects) is accreted in a stream onto the halo, but the stream velocity induces a velocity gradient in a preferential direction in that region perpendicular to the infall stream. This results in
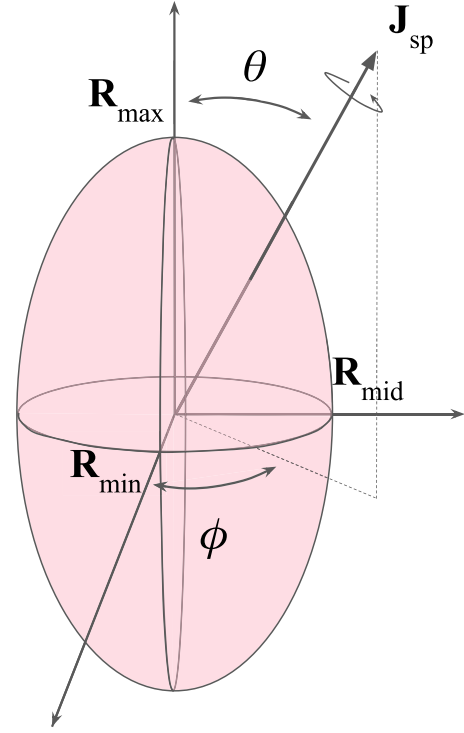

Figure 8. Ellipsoid in spherical coordinates for an arbitrary spin vector direction. Coordinates are chosen such that the primary axes of the ellipsoid are aligned along the Cartesian coordinate directions, with R_{max}, the polar radius of the prolate spheroid, along the z-axis. The spin vector (Equation (9)) can be aligned in any direction with respect to the ellipsoid axes, and its relative alignment with respect to these axes is described by the usual spherical angular coordinates θ and ϕ.

spinning top rotator behavior, depicted also in a cartoon at the bottom of Figure 9.

SIGOs, however, exhibit a weak bimodal distribution of alignment with R_{max}. The majority are preferentially misaligned with the maximum axis, while some demonstrate alignment as in the case of the DM GHOSts described above. Considering an idealized growth scenario, SIGOs are embedded in the gas stream, which is normally in the process of accreting onto a DM halo. This configuration often yields an R_{max} in alignment with the accretion stream, (as is the case in the example in Figure 1). As described above with DM GHOSts, the stream velocity induces a velocity gradient (in our case toward the x-direction), which may be perpendicular to the infall stream moving in the y- or z-directions. (For example, see Figure 3 in Lake et al. 2023, where a SIGO is embedded in a stream of gas infalling toward a larger halo. All the gas in the region is moving toward this stream, however greater velocities are found on the $+x$ side, a gradient induced by the original stream velocity in the $+x$-direction.) This perpendicular accretion mode causes objects to have alignment between $\boldsymbol{J}_{\mathrm{sp}}$ and $\boldsymbol{R}_{\mathrm{max}}$. However, this picture is idealized, and in practice the SIGOs represent a density perturbation within the stream that results in gas accretion that is not necessarily aligned with the object's R_{max}. Those SIGOs that are preferentially misaligned respect to R_{max} show a variety of alignments with respect to R_{min}. This is potentially due to the fact that (as opposed to the oblate case described above) for prolate spheroids, the system's symmetry is such that $R_{\mathrm{min}} \sim R_{\mathrm{mid}}$.

The similarity between the DM and gas components in Figure 9 is further investigated below. Specifically, we
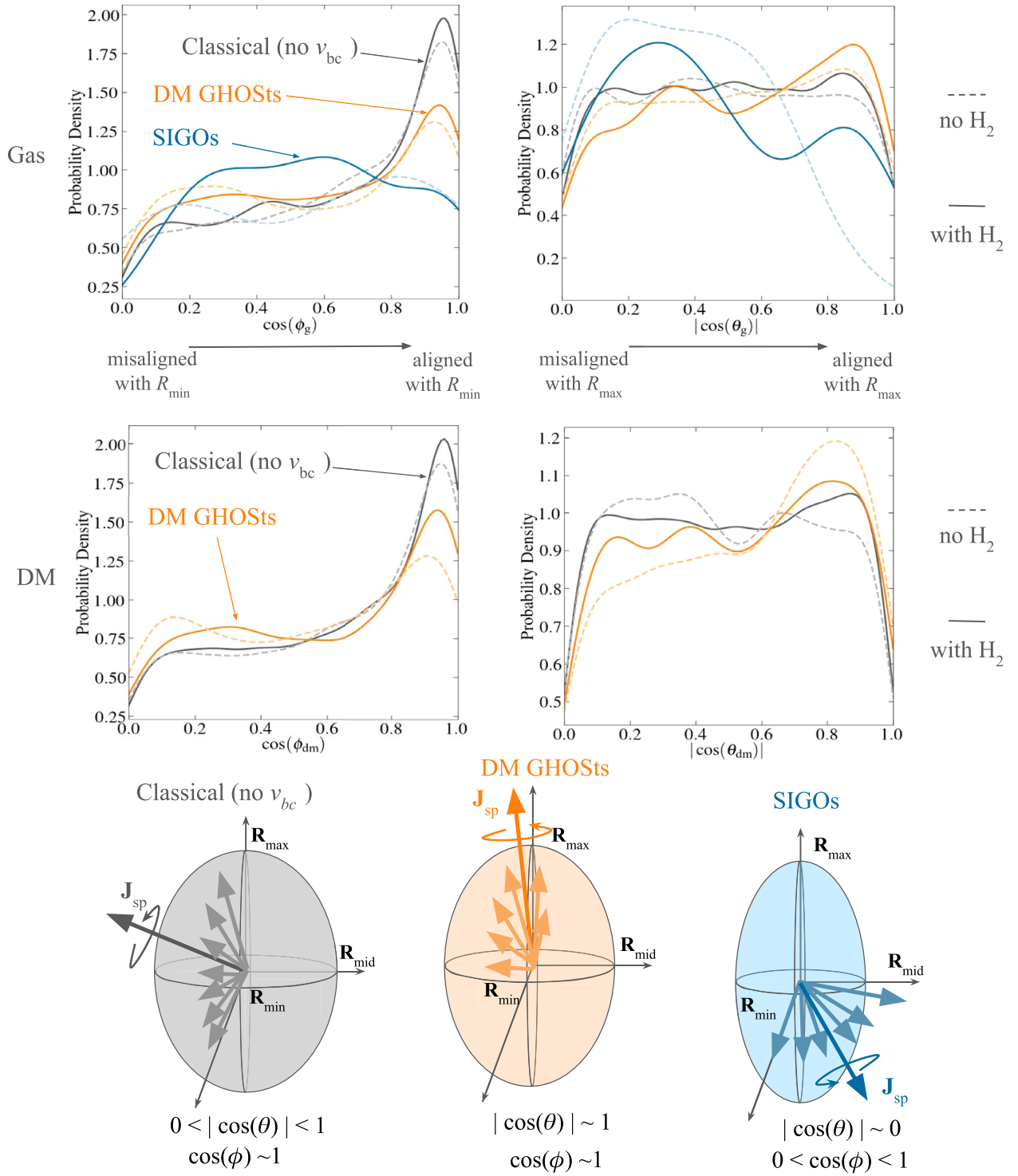
Figure 9. Top panels: left: probability density distribution of $\cos(\phi_g)$, the angle between R_{min} and the spin vector of the gas component of GP objects (see Figure 2). Right: probability density distribution of $|\cos(\theta_g)|$, the angle between R_{max} and the spin vector. The darker lines denote runs with H_2 cooling, while the lighter dashed lines denote no cooling. The distributions are separated into the object classes listed in Table 2 and calculated using a Gaussian kernel density. The orange distributions include the gas component of DM GHOSts, the gray distributions show the gas component of classical halos without v_{bc}, and the blue distributions show SIGOs. Middle panels: left: probability density distribution of $\cos(\phi_{dm})$, the angle between R_{min} and the spin vector of the DM component of objects (see Figure 2). Right: probability density distribution of $|\cos(\theta_{dm})|$, the angle between R_{max} and the spin vector. The darker lines denote runs with H_2 cooling, while the lighter dashed lines denote no cooling. The distributions are separated into the object classes listed in Table 2 and calculated using a Gaussian kernel density. The orange distributions include the gas component of DM GHOSts and the gray distributions show the gas component of classical halos without v_{bc}. SIGOs, which have little to no DM component, are not shown. Bottom panels: cartoon depiction of the orientation of the spin vector with respect to the various object classes: classical halos (left), DM GHOSts (middle), and SIGOs (right). The large, dark arrow indicates the most common orientation, while the other faint arrows indicate a spread of other common alignments for each object type according to the distributions in the top and middle panels.
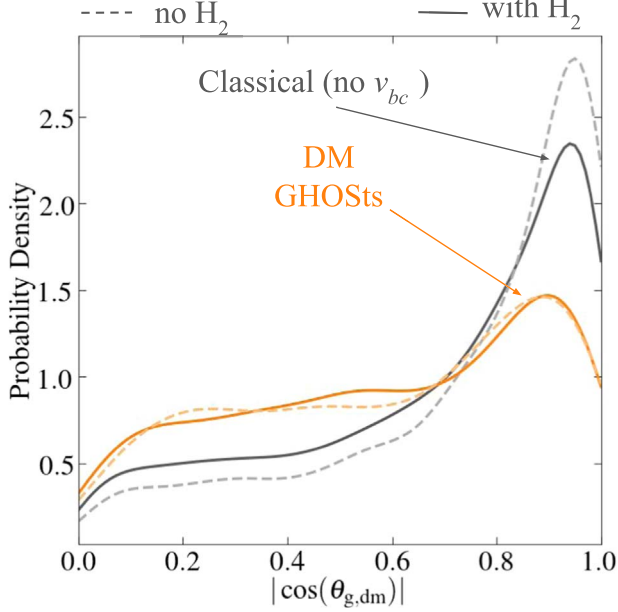
11

Figure 10. Probability density distribution of the cosine of the misalignment between the spin parameter of the gas and DM components of individual GP objects (see Equation (12)). The gray distributions are classical halos, the orange distributions are DM GHOSts, and the blue dashed distributions show SIGOs. The darker lines denote no cooling, while the lighter dashed lines show the inclusion of molecular cooling.

calculate the misalignment angle between the angular momentum of the DM component and the gas component,

$$\cos(\theta_{\rm g,DM}) = \frac{\boldsymbol{J}_{\rm DM} \cdot \boldsymbol{J}_{\rm g}}{|J_{\rm DM}||J_{\rm g}|}. \tag{12}$$

Note that for SIGOs the DM component is negligible, thus we only consider classical objects and DM GHOSts in this analysis. Figure 10 shows probability distributions of $\cos(\theta_{\rm g,DM})$. Consistent with previous studies (e.g., Chiou et al. 2018), the classical halos have a strong alignment between the gas and DM components. On the other hand, the alignment between the gas and DM spin is weaker for DM GHOSts, with a long tail of nearly isotropic configurations. This result is consistent between molecular and atomic cooling. In future work it may also be relevant to examine the effects of feedback on this distribution. This may especially be relevant for star-forming SIGOs.

3.3. Rotation Curves and Mass Distribution of DM GHOSts

Because the stream velocity affects the angular momentum and morphological configuration of structures, we expect a possible effect on the density distribution and rotational curves. In particular, since rotation curves contain signatures of the DM component, we expect that both SIGOs and DM GHOSts will deviate from the classical profiles.

In particular, in this section we focus our analysis to a comparison between runs with and without the stream velocity (0vH2 and 2vH2). Figure 11 shows the density of gas of DM GHOSts (top panel) and classical halos (bottom panel) as a function of radius from the center of mass, with an NFW (e.g., Navarro et al. 1996a, 1996b, 1997) halo profile overplotted (dashed line). The stream velocity serves to reduce densities across the structure, as expected. Physically, this is due to the
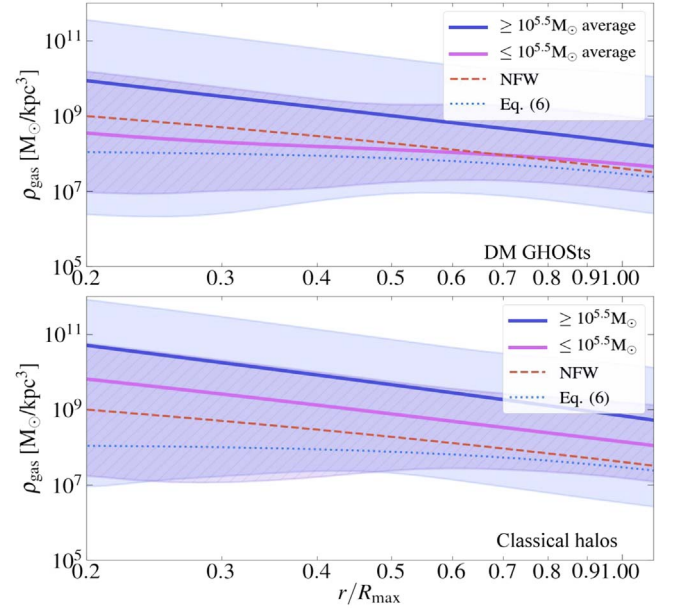

Figure 11. Density of gas in DM GHOSts as a function of radius, normalized to $R_{\rm max}$ of the ellipsoid, for the molecular cooling run with $v_{\rm bc} = 2\sigma_{v_{\rm bc}}$ (top panel) compared to classical halos with $v_{\rm bc} = 0\sigma_{v_{\rm bc}}$ and molecular cooling (bottom panel). The density is calculated in 50 ellipsoidal shells moving out from the center of the object. We split objects by mass–the average rotation curve for objects above $10^{5.5}~M_{\odot}$ is shown in solid blue, while those below this cutoff are plotted in solid pink. Low-mass objects display a deviation from the classical rotation curves, with less of a cusp. The blue shaded region shows 1σ away from the curve for objects above $10^{5.5}~M_{\odot}$, while the purple hatched region shows 1σ away from the curve for objects below $10^{5.5}~M_{\odot}$. An NFW profile for a $10^5~M_{\odot}$ halo is shown for comparison as the dashed line. Equation (6) is plotted for a gas object with average density in solid blue.

advection of gas from the halo and the spatial separation of the two components. In addition, at low masses ($\lesssim 10^{5.5}~M_{\odot}$), we observe a deviation from the NFW shape, with a constant, core profile, rather than a cusp. Using the prolate density profile, Equation (6), we see that a core-like structure is expected for these ellipsoids (solid line). In Section 3.1.2, we demonstrated that low-mass objects had high eccentricities. Since the classical NFW formulation assumes spherical overdensities (e.g., Navarro et al. 1996a, 1996b, 1997), another reason for the deviation may be the extreme eccentricities of very-low-mass objects in the stream velocity simulations.

Figure 12 shows the rotation curves of DM GHOSts (top panel) and classical halos (bottom panel). The rotation curves as a function of radius for DM GHOSts have two behaviors separated by mass. In particular, the core-type density distribution of low-mass objects in the stream also means that their rotational velocities do not climb as fast.

DM GHOSts are more diffuse and rotationally supported than classical halos, having received a boost from the stream velocity. In Figure 13, we show the velocity at $R_{\rm max}$ as a function of the total mass. We compare this to the nominal NFW expectation, following Navarro et al. (1997), taking the maximum of the NFW circular velocity,

$$v_{\rm circ}^2 = \frac{1}{x} \frac{\ln(1 + cx) - (cx)/(1 + cx)}{\ln(1 + c) - c/(1 + c)}, \tag{13}$$

where $x = r/r_{200}$ and c is the halo concentration. When molecular cooling is included, the velocity at $R_{\rm max}$ exceeds the NFW circular velocity because the cooling process allows gas to condense to smaller radii. In addition to the cooling effect,
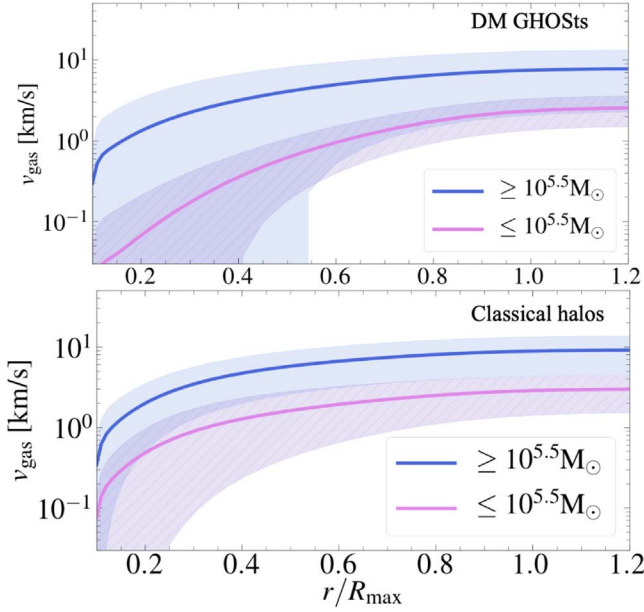
Figure 12. Rotation curves of DM GHOSts as a function of radius, calculated in ellipsoidal shells going outward, for the molecular cooling run with $v_{bc} = 2\sigma_{v_{bc}}$ (top panel) and $v_{bc} = 0\sigma_{v_{bc}}$ (bottom panel). The average velocity of the gas in an ellipsoidal shell at each radius is normalized by v_{circ}, the circular radius at R_{max} of the ellipsoid. The objects are colored by the mass of their gas component. We split objects by mass—the average rotation curve for objects above $10^{5.5}\,M_{\odot}$ is shown in solid blue, while those below this cutoff are plotted in solid pink. Low-mass objects display a deviation from the classical rotation curves, with less of a cusp. The blue shaded region shows 1σ away from the curve for objects above $10^{5.5}\,M_{\odot}$, while the purple hatched region shows 1σ away from the curve for objects below $10^{5.5}\,M_{\odot}$.
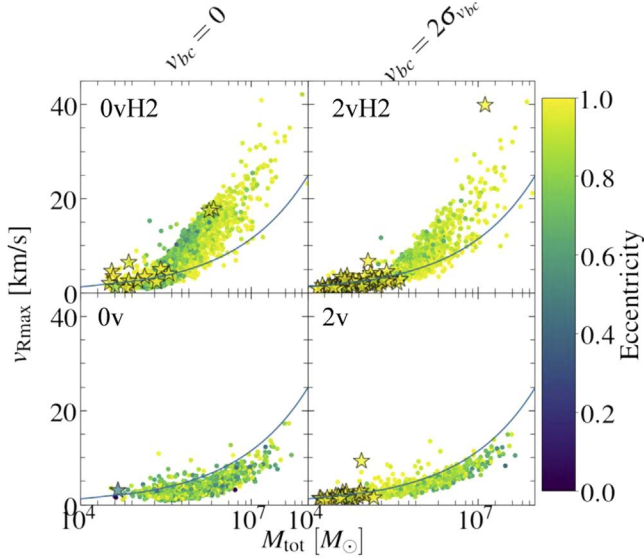
Figure 13. Scatterplot of the velocity at R_{max} (v_{Rmax}) of objects as a function of total mass (M_{tot}). The top two panels show the molecular cooling runs, and the bottom two panels show no cooling. The left column has no stream velocity and the right column is from $v_{bc} = 2\sigma_{v_{bc}}$. Stars represent SIGOs, as defined in Section 2.3. The color bar shows the eccentricity (Equation (3)). The solid blue line shows the expected value for an NFW profile.

the stream velocity also boosts the gas velocity. In regions of streaming, the velocity at R_{max} reaches or exceeds the expected values compared to regions without streaming. This behavior is expected based on their larger overall spin parameters than in the classical case as seen in Figure 6.
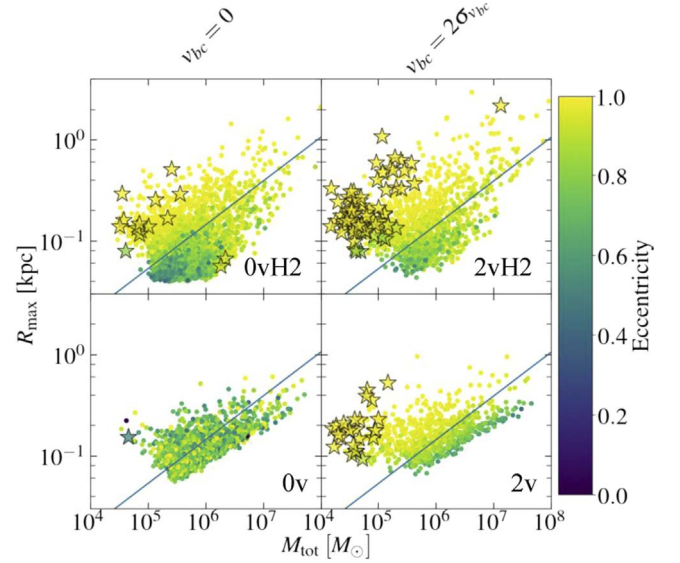

Figure 14. Scatterplot of the R_{max} of objects as a function of total mass (M_{tot}). The top two panels show the molecular cooling runs, and the bottom two panels show no cooling. The left column has no stream velocity and the right column is from $v_{bc} = 2\sigma_{v_{bc}}$. Stars represent SIGOs, as defined in Section 2.3. There are a few objects misclassified as SIGOs in the runs with no stream velocity—see Appendix A for a discussion. The color bar shows the eccentricity (Equation (3)). The solid blue line shows the expected value for an NFW profile. For the 0vH2 run, 22% of objects fall above the expected NFW line. For the 2vH2 run, this fraction rises to 58% of objects located above the line.

We note that the radii of DM GHOSts and SIGOs are larger than those expected from classical considerations. Specifically, in Figure 14, the maximum ellipsoid radius is plotted against the total mass of the object, with the NFW expected relationship overplotted. The H$_2$ cooling runs show objects which have condensed to smaller maximum radii (top left panel). We calculate the fraction of objects in Figure 14 above and below the NFW line, and find that the majority (~80%) of classical halos condense to smaller radii than the NFW R_{max} with H$_2$ cooling in regions of no stream velocity. In the presence of stream velocity, however, the velocity boost overall yields larger radii (top right panel). In the 2vH2 run, 60% of all objects lie above the line, having larger than expected maximum radii. Interestingly, SIGOs tend to have higher R_{max} than the NFW profile in all cases. Again, we suggest that eccentricity plays a central role in giving objects much greater R_{max} than would be possible in the spherical case.

These results illustrate the combined effects of the stream velocity and molecular cooling that cause DM GHOSts to be more diffuse and rotationally supported than their classical counterparts of similar masses.

4. Discussion

In this work, we investigate the spin, rotation, and morphological properties of structures in the presence of the stream velocity at $z = 20$ using high-resolution numerical simulations in AREPO. For the first time, molecular cooling is included in a detailed study of these dynamical properties. We focus on a class of objects that we term DM GHOSts, structures where the baryonic component is offset from the DM halo, but does not fully escape the virial radius (as with SIGOs, which were previously the focus of studies by the Supersonic Project). As in Figure 1, we emphasize that as time goes by, the gas

sinks to the center of the DM halo, but carries the signature of its unique formation channel. Using molecular cooling simulations, we are able to constrain the properties of SIGOs and DM GHOSts more precisely in comparison to classical low-mass objects than was possible in previous studies (e.g., Chiou et al. 2018).

We considered the following physical properties of DM GHOSts, comparing them to classical objects and SIGOs.

1. Morphology: we show that SIGOs are the most elongated class of objects, followed by DM GHOSts, for both the gas and DM components (as depicted in Figures 3 and 4). We note that the DM component of DM GHOSts is significantly elongated compared to that of the classical objects. Frequently, SIGOs and DM GHOSts tend to be prolate ellipsoidal, and we present an analytical expression of their gravitational potential. While the gas morphology deviates from spherical symmetry, star formation takes place at density peaks, which ends up as less-elongated ellipsoids (W. Lake et al. 2023, in preparation).

   Interestingly, we find that the DM component of DM GHOSts is elongated as well, unlike the classical (no stream velocity) counterparts. This prediction may be observable with gravitational lensing models that allow for deviation from spherical symmetry (e.g., Kneib & Natarajan 2011). Note that while there is no direct correlation between the large-scale stream velocity distribution and the density field, the stream velocity divergence relates to the density field via the continuity equation (e.g., Tseliakhovich & Hirata 2010; Tseliakhovich et al. 2011). Thus, high-density σ peaks are weakly correlated with large stream velocity patches, e.g., Fialkov (2014). The box considered here has an increased σ_8 compared to the average. Thus, it roughly corresponds to a high-redshift progenitor of a patch of the universe within a density peak such as the Virgo cluster (e.g., Naoz & Barkana 2007). Thus, because of the above weak correlation, we expect that galaxy clusters are likely to host elongated DM substructures. Thus, given the right alignments, they may be detected using strong lensing (e.g., Mahler et al. 2023). We emphasize that about 40% of the universe has a stream velocity larger that $1\sigma_{vbc}$, and therefore, DM GOHSts with elongated gas and DM components should be common regardless of large-scale density fluctuations.

2. Spin Parameter: the stream velocity serves to increase the total angular momentum and thus rotational support of SIGOs and DM GHOSts. As shown in Figure 6, DM GHOSts have a higher gas spin parameter compared to classical objects. Less spherical objects (more eccentric objects) have greater angular momenta; see Figure 7.

   As expected, the spin vectors of classical gas objects are aligned with those objects' minimum radii, forming a puffy disk-like configuration at high redshift, consistent with lower-redshift analyses of larger objects (e.g., Jesseit 2004; Kautsch et al. 2006; Wheeler et al. 2017; El-Badry et al. 2018). DM GHOSts, on the other hand, demonstrate spin vectors that are often aligned with their maximum axis (similar to a "spinning top," see Figure 9). Lastly, SIGOs' total gas angular momenta exhibit a weak bifurcation. Most are misaligned with the maximum radius without a preference for alignment with the minimum radius, while another group are aligned toward the maximum radius (similarly to DM GHOSts, as shown in Figure 9).

   Additionally, the DM and gas components' spins in classical halos are almost always aligned. However, DM GHOSts, as shown in Figure 10, have a weak preference for alignment between the DM's and gas's spins, with a long tail of nearly isotropic configurations.

3. Mass distribution: classical objects are expected to have a cusp-like mass distribution (e.g., Navarro et al. 1996a), which are often reproduced in simulations (e.g., Delos & White 2023). The stream velocity reduces the densities of objects and increases their sizes, causing them to be puffier and more diffuse than classical objects and the theoretical NFW profile. The ellipsoid-like configuration of low-mass DM GHOSts yields a core-like profile (see Figure 11). As expected, SIGOs that follow an ellipsoid profile have a core-like mass density, with a nearly constant density (see Figure 20 in Appendix C). This behavior for SIGOs is consistent with the suggestion that SIGOs are giant molecular cloud analogs (Lake et al. 2023).

4. Rotation curves: the stream velocity affects not only the spin parameter, but also the rotational velocity curves of structures. Objects formed by streaming have a higher maximum rotational velocity than those formed without for a given mass (see Figures 12 and 13). Furthermore, the bifurcation between high- and low-mass objects seen in the radial mass distributions for DM GHOSts is also reflected in their velocity profiles. Low-mass ($\lesssim 10^{5.5}\,M_\odot$) objects, which have cores, do not reach high rotational velocities at their inner radii. The inclusion of molecular cooling increases the velocity at the maximum radius and decreases the maximum radius by condensing rotationally supported material inward.

   We note that rotational curve anomalies have been observed for slightly larger objects in the local universe (e.g., Sales et al. 2022). We speculate that anomalous rotation curves produced by the stream velocity at high redshift may persist to low-redshift structures. This may be related to the observed "diversity of rotation curves" problem for ultra-faint dwarf galaxies.

The combined effects of molecular cooling and the stream velocity give the most accurate picture to date of the morphological and rotational properties of DM GHOSts. We characterize these objects as highly diffuse, rotationally supported dwarf structures with large radii and high eccentricities. Based on these anomalous properties, we speculate that at low redshift, DM GHOSts may evolve to form some ultra-faint dwarf galaxies or anomalous dwarf galaxies. In particular, some dwarf galaxies exhibit similar properties, including a diffuse structure and atypical rotation curves (e.g., Bullock & Boylan-Kolchin 2017; Sales et al. 2022). Thus, while observed ultra-faint dwarf galaxies and dwarf galaxies may be more massive than DM GHOSts, we find they share similar characteristics at these high redshifts. We expect DM GHOSts to grow over time according to the natural hierarchical growth of structure, and may be the progenitors of some faint dwarf galaxies in regions of the universe with a highly supersonic stream velocity at early times.

Appendix A
Choice of Cutoff Gas Fraction

In the first papers by the Supersonic Project that included only adiabatic or atomic cooling (e.g., Popa et al. 2016; Chiou et al. 2018, 2019, 2021; Lake et al. 2021), a cutoff gas fraction of $f_g = 0.4$ was chosen for the definition of SIGOs. Those studies' statistics for SIGO abundances and properties were thus calculated for objects that were located outside of the virial radius of their parent DM halo and had $f_g = 0.4$ within the bounds of the ellipsoid fit described in Section 2.3. This choice of gas fraction was a somewhat arbitrary choice, motivated by the fact that it was above the cosmic baryon fraction and close to the stellar fraction of globular clusters (Chiou et al. 2018). Nakazato et al. (2022) found that in molecular cooling simulations, this choice was too lenient, and resulted in the identification of SIGOs in runs without the stream velocity.

We also find that a choice of $f_g = 0.4$ results in an unacceptable number of objects being identified as SIGOs in molecular cooling simulations. For example, Figure 15 shows the eccentricity versus mass of objects, as in Figure 5, with gas fractions of 0.4 (left), 0.5 (center), and 0.6 (right). The top left panel shows the molecular cooling run with no stream velocity, and stars represent SIGOs. With $f_g = 0.4$ and $f_g = 0.5$, there are many objects identified as SIGOs by the algorithm. While these gas-rich structures may be interesting, they are obviously not the result of a large stream velocity. In order to exclude as many of these false SIGOs as possible while still having plenty of objects in the 2v runs to study, we follow Nakazato et al. (2022) and choose $f_g = 0.6$ for this work.

For completeness, Figures 16 and 17 show the probability density distributions for GP objects from this work (as in Figures 3, 6, 9, and 10) with varying gas fraction from the previous value of 0.4 to the value of 0.6 adopted in this work. The results are generally consistent despite changing the gas fraction cutoff.
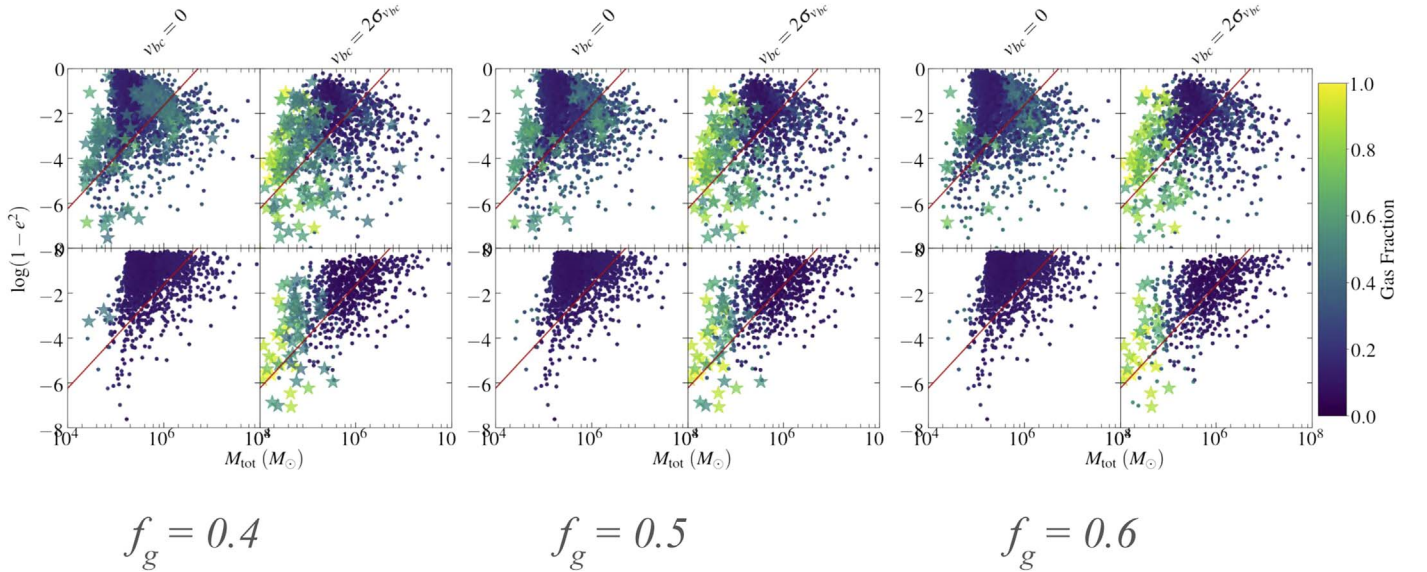

Figure 15. Same as Figure 5 (scatterplot of $\log(1 - e^2)$ vs. M_{tot} for GP objects,), with the definition of SIGOs calculated using gas fractions of 0.4 (left), 0.5 (center), and 0.6 (right). Significantly more SIGOs are found in the molecular cooling runs without the stream velocity (top left of each panel) for $f_g = 0.4$ and $f_g = 0.5$, as was also shown in Nakazato et al. (2022). As in Figure 5, the top two panels show the H_2 cooling runs, and the bottom two panels show runs without cooling. The left column has no stream velocity and the right column is from the $v_{bc} = 2\sigma_{v_{bc}}$ runs. Stars represent SIGOs, as defined in Section 2.3. The color bar shows the gas fraction (Equation (1)). The red overplotted line is the expected relationship from Equation (8) for an example object with the average density and maximum radius of objects in the H_2 cooling runs ($\bar{\rho}_{R\,max} = 1.8 \times 10^8 M_\odot \, kpc^{-3}$ and $\bar{R}_{max} = 0.134$ kpc).
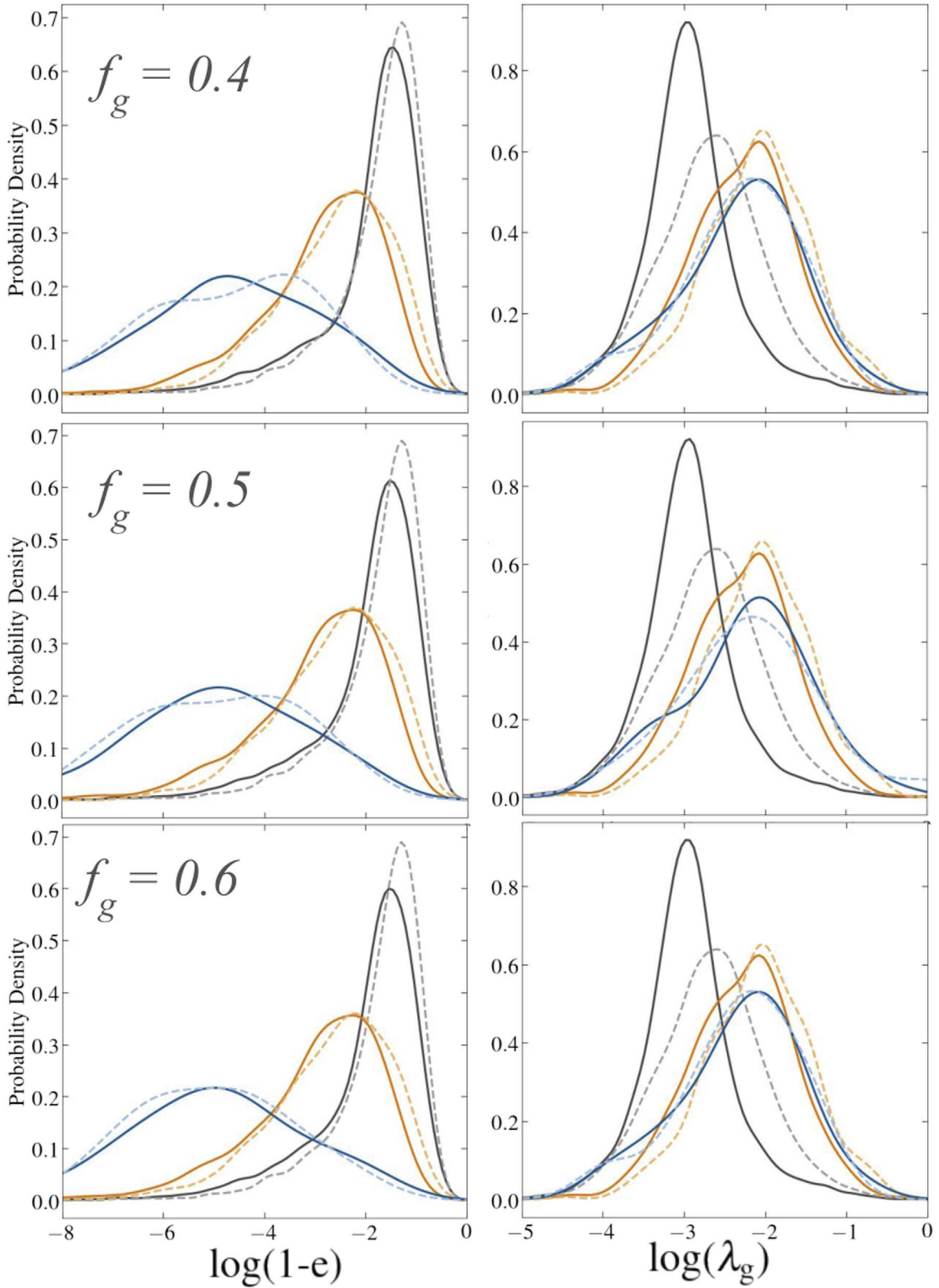
Figure 16. Probability density distributions as shown in Figure 3 ($\log(1 - e)$, where e is the eccentricity (Equation (3)), for GP objects) and Figure 6 (λ_g for GP objects), with the definition of SIGOs calculated using gas fractions of 0.4 (top row), 0.5 (center row), and 0.6 (bottom row). As seen in Figure 15, more SIGOs are found in the molecular cooling runs without the stream velocity for $f_g = 0.4$ and $f_g = 0.5$, as was also shown in Nakazato et al. (2022), which motivates us to choose a gas fraction in this work of 0.6. However, the results are broadly consistent despite variations in the gas fraction, and the effects are only seen in the distribution of SIGOs. As in Figures 5 and 6, the distributions are separated into the object classes listed in Table 2 and calculated using a Gaussian kernel density. The orange distributions include the gas component of DM GHOSts, the gray distributions show the gas component of classical halos without v_{bc}, and the blue distributions show SIGOs.
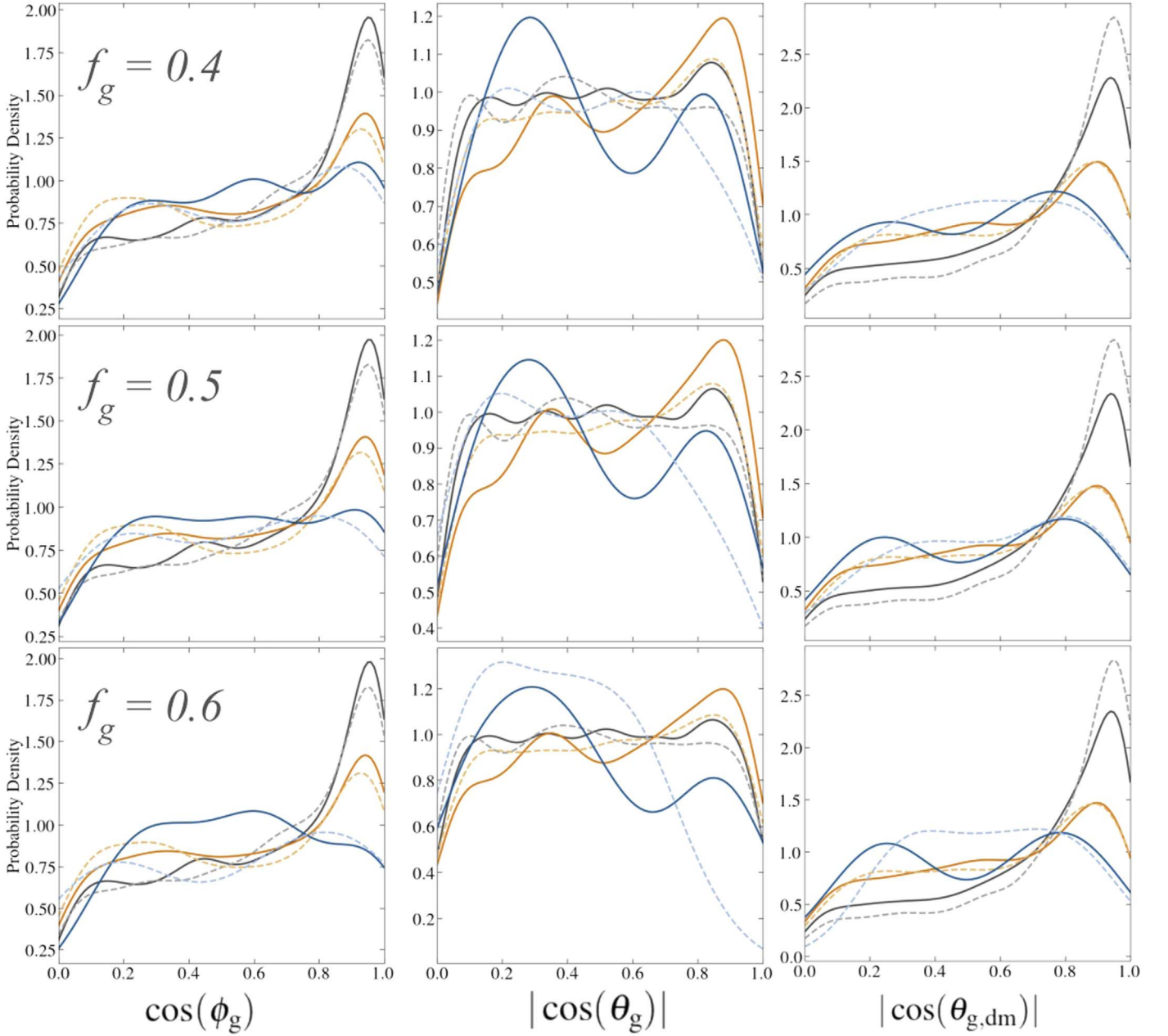
Figure 17. Probability density distributions as shown in Figure 9 (left: $\cos\phi_g$, the angle between R_{min} and the spin vector of the gas component of GP objects; see Figure 2. Center: $|\cos(\theta_g)|$, the angle between R_{max} and the spin vector) and Figure 10 (right: $|\cos\theta_{g,dm}|$, the misalignment between the spin parameter of the gas and DM components of individual objects), with the definition of SIGOs calculated using gas fractions of 0.4 (top row), 0.5 (center row), and 0.6 (bottom row). As seen in Figure 15, more SIGOs are found in the molecular cooling runs without the stream velocity for $f_g = 0.4$ and $f_g = 0.5$, as was also shown in Nakazato et al. (2022), which motivates us to choose in this work a gas fraction of 0.6. However, the results are broadly consistent despite variations in the gas fraction, and the effects are only seen in the distribution of SIGOS. As before, the darker lines denote runs with H_2 cooling, while the lighter dashed lines denote no cooling. The distributions are separated into the object classes listed in Table 2 and calculated using a Gaussian kernel density. The orange distributions include the gas component of DM GHOSts, the gray distributions show the gas component of classical halos without v_{bc}, and the blue distributions show SIGOs.

Appendix B
Derivation of the Prolate Ellipsoidal Potential

In this Appendix, we present a derivation of the gravitational potential and total mass of prolate spheroids. Binney & Tremaine (2008) give the general formulae for the potentials of various ellipsoidal bodies in their Table 2.1. The following equations apply to any inhomogeneous ellipsoid with axes a_1, a_2, and a_3. The potential is,

$$\Phi(\boldsymbol{x}) = -\pi G \frac{a_2 a_3}{a_1} \int_0^\infty \frac{d\tau}{\Delta} \{\varphi(\infty) - \varphi[m(\tau, \boldsymbol{x})]\}, \quad \text{(B1)}$$

where,

$$\Delta^2(\tau) \equiv \prod_{i=1}^{3} (a_i^2 + \tau), \quad \text{(B2)}$$

$$m^2(\tau, \boldsymbol{x}) \equiv a_1^2 \sum_{i=1}^{3} \frac{x_i^2}{a_i^2 + \tau} \quad \text{(B3)}$$

,and,

$$\varphi(m) \equiv \int_0^{m^2} \rho(\boldsymbol{x}) dm^2(0, \boldsymbol{x}). \quad \text{(B4)}$$

For the prolate spheroidal case, we have,

$$a_1 = a_2 = R_{\min} \quad \text{(B5)}$$

,and,

$$a_3 = R_{\max}. \quad \text{(B6)}$$

Thus, in cylindrical coordinates (R, z),

$$m^2(\tau, \boldsymbol{x}) = R_{\min}^2 \left[\frac{R^2}{R_{\min}^2 + \tau} + \frac{z^2}{R_{\max}^2 + \tau} \right], \quad \text{(B7)}$$

and from Equation (B2),

$$\Delta^2(\tau) = (R_{\min}^2 + \tau)^2 (R_{\max}^2 + \tau). \quad \text{(B8)}$$

Equation (B4) requires a density distribution, and here we will use the following prolate spheroidal density distribution,

$$\rho(m^2) = \rho_0 \left(1 + \left(\frac{m}{a_0} \right)^2 \right)^{-\frac{3}{2}}, \quad \text{(B9)}$$

where ρ_0 and a_0 are constants.

Plugging the density from Equation (B9) into Equation (B4) gives,

$$\varphi(m) = \int_0^{m^2} \rho_0 \left[1 + \left(\frac{m}{a_0} \right)^2 \right]^{-3/2} dm^2(0, \boldsymbol{x}) \quad \text{(B10)}$$

,

$$= -2a_0^2 \rho_0 \left[1 + \left(\frac{m(0, \boldsymbol{x})}{a_0} \right)^2 \right]^{-1/2} + 2a_0^2 \rho_0. \quad \text{(B11)}$$

Additionally,

$$\varphi(\infty) = 2a_0^2 \rho_0 \quad \text{(B12)}$$

.From in Equations (B1), (B7), (B8), (B11), and (B12), the prolate potential is,

$$\Phi(\boldsymbol{x}) = -2\pi G R_{\max} a_0^2 \rho_0 \int_0^\infty \frac{d\tau}{(R_{\min}^2 + \tau)\sqrt{R_{\max}^2 + \tau}} $$
$$\times \left[1 + \left(\frac{m(0, \boldsymbol{x})}{a_0} \right)^2 \right]^{-1/2}. \quad \text{(B13)}$$

And with Equation (B7), we have Equation (B1) thus evaluates to,

$$\Phi(\boldsymbol{x}) = -2\pi G R_{\max} a_0^2 \rho_0 \int_0^\infty \frac{d\tau}{(R_{\min}^2 + \tau)\sqrt{R_{\max}^2 + \tau}} \left[1 + \left(\frac{R_{\min}^2}{a_0^2} \right. \right.$$
$$\times \left. \left. \left[\frac{R^2}{R_{\min}^2} + \frac{z^2}{R_{\max}^2} \right] \right) \right]^{-1/2}. \quad \text{(B14)}$$

Evaluating the integral, we get,

$$\Phi(\boldsymbol{x}) = -4\pi G R_{\max}^2 a_0^3 \rho_0 \left(\frac{\cos^{-1}\left(\frac{R_{\max}}{R_{\min}} \right)}{\sqrt{R_{\max}^2 - R_{\min}^2}} \right)$$
$$\times \frac{1}{\sqrt{1 + \left(\frac{R_{\min}^2}{a_0^2} \left[\frac{R^2}{R_{\min}^2} + \frac{z^2}{R_{\max}^2} \right] \right)}}. \quad \text{(B15)}$$

Taking $a_0 = R_{\max}$,

$$\Phi(\boldsymbol{x}) = -\frac{4\pi G R_{\max}^4 \rho_0 \cos^{-1}(\sqrt{1 - e^2})}{e\sqrt{1 + (1 - e^2)\left(\frac{R^2}{R_{\min}^2} + \frac{z^2}{R_{\max}^2} \right)}}. \quad \text{(B16)}$$

Now, we find the dependence of the total mass on eccentricity, starting with a similar argument to that presented in Binney & Tremaine (2008) for the potential of oblate spheroids. In cylindrical coordinates a prolate spheroidal shell with axes $\beta R_{\max}$ and $\beta R_{\min}$ is given by,

$$\frac{R^2}{R_{\min}^2} + \frac{z^2}{R_{\max}^2} = \beta^2. \quad \text{(B17)}$$

Here, the z-axis is aligned with the polar radius ($R_{\max}$) and the R-coordinate points in the direction of the equatorial radius ($R_{\min}$). The volume enclosed inside this shell is given by,

$$V = \frac{4}{3}\pi R_{\max} R_{\min}^2 \beta^3 \quad \text{(B18)}$$

,

$$= \frac{4}{3}\pi R_{\max}^3 \beta^3 (1 - e^2) \quad \text{(B19)}$$

.Thus, assuming a constant surface density, the mass enclosed between two shells β and $\beta + \delta\beta$ is,

$$\delta M = 4\pi \rho R_{\max}^3 (1 - e^2)\beta^2 \delta\beta \quad \text{(B20)}$$

.The full mass of the ellipsoid is found by integrating over a set of similar spheroids from the center to the outer edge of the object. Using the notation of Binney & Tremaine (2008), this

set is given by all the spheroids for which,

$$\text{constant} = m^2 \equiv \frac{R^2}{1 - e^2} + z^2. \qquad (B21)$$

This give a constant $m = \beta R_{max}$. Thus, for some density function $\rho(m^2)$, according to Equation (B20),

$$\delta M = 4\pi\rho(m^2)(1 - e^2)m^2\delta m. \qquad (B22)$$

Integrating this equation over the ellipsoid gives the total mass,

$$M = 4\pi(1 - e^2) \int_0^{R_{max}} \rho(m^2)m^2 dm. \qquad (B23)$$

Once again, we assume the density distribution of Equation (6), and plugging into Equation (B23), we solve,

$$M = 4\pi(1 - e^2) \int_0^{R_{max}} \left(1 + \left(\frac{m}{a_0}\right)^2\right)^{-\frac{3}{2}} m^2 dm, \qquad (B24)$$

to obtain,

$$M = 4\pi\rho_0(1 - e^2)a_0^3\left[\sinh^{-1}\left(\frac{R_{max}}{a_0}\right) - \frac{R_{max}}{\sqrt{a_0^2 + R_{max}^2}}\right]. \qquad (B25)$$

Taking $a_0 = R_{max}$ as above gives,

$$M = 4\pi\rho_0(1 - e^2)R_{max}^3\left(\sinh^{-1}(1) - \frac{1}{\sqrt{2}}\right) \qquad (B26)$$

,

$$\approx 2.19\rho_0(1 - e^2)R_{max}^3.$$

Appendix C
Morphological Investigation

In this Appendix, we include several supporting figures related to our morphological and rotational investigation above.

In Figure 18, we plot the probability density distributions of the three axis ratios plotted on the axes of Figure 3. The classical halos tendency toward sphericity ($R_{min}/R_{mid} \sim R_{min}/R_{max} \sim R_{mid}/R_{max} \sim 1$) is clearly seen here, as well as the distinct deviation of SIGOs and DM GHOSts away from sphericity. For SIGOs especially, the distributions show evidence of triaxiality ($R_{min}/R_{mid} \neq R_{min}/R_{max} \neq R_{mid}/R_{max}$). Figure 18 also shows the axis ratios for DM-primary objects (bottom row). Here, we see that the DM components of DM GHOSts are not only more eccentric, having a tail of small axis ratios as in Figure 3, but also show prolate shapes when R_{mid} is taken into account. In the center bottom panel, the ratio
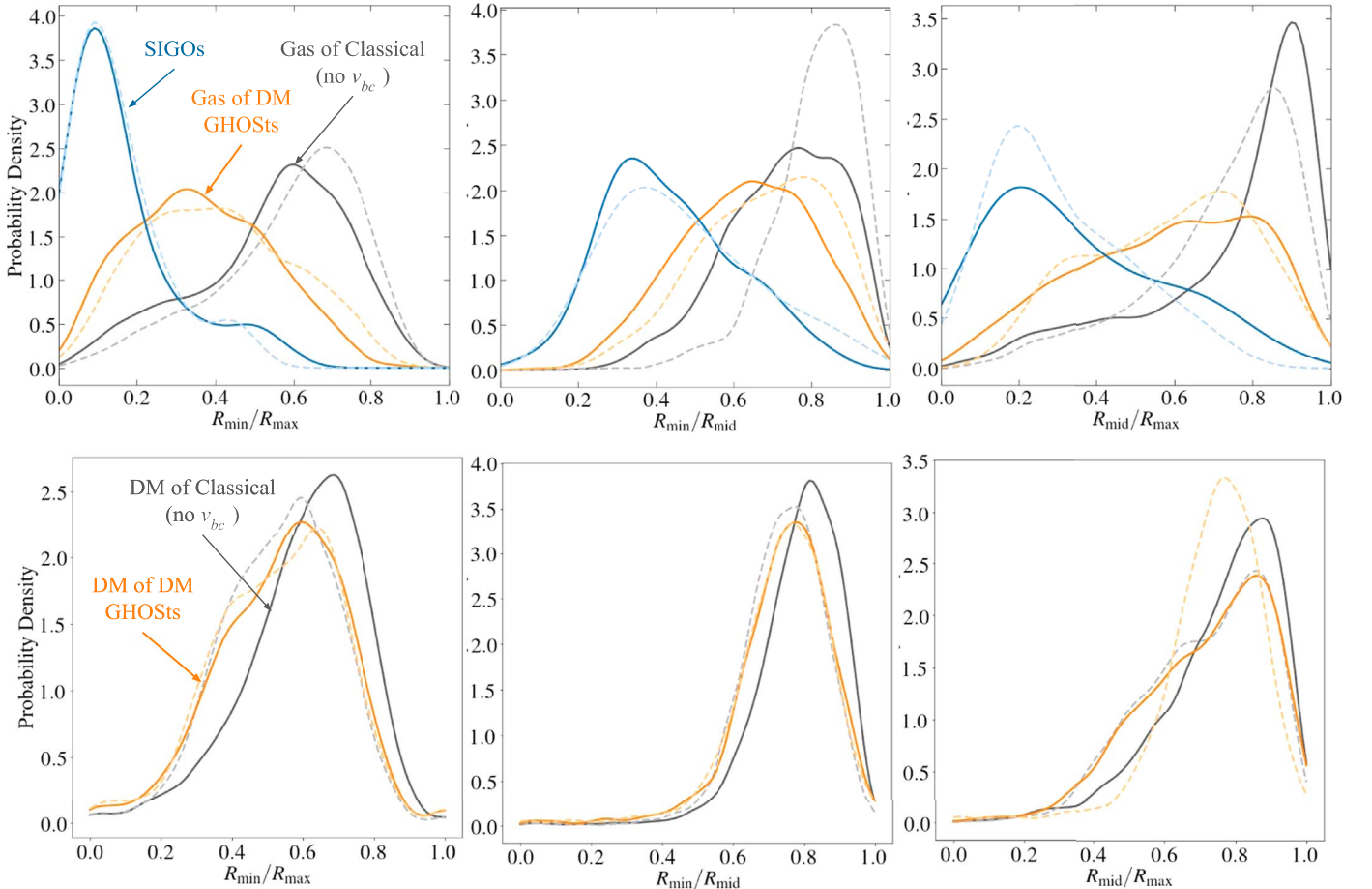

Figure 18. Probability density distribution of the ratios of GP objects. Following the same convention as in Figure 3, the various distributions demonstrate runs with and without the stream velocity and cooling. The orange distributions show objects with a gas fraction f of less than 0.6 in the runs without the stream velocity ($v_{bc} = 0\sigma_{v_{bc}}$), the gray distributions show the classical equivalent of $f < 0.6$ objects in the $v_{bc} = 0\sigma_{v_{bc}}$ run, and the blue dashed distributions show SIGOs, which are only found in the $v_{bc} = 2\sigma_{v_{bc}}$ run. The darker lines denote no cooling, while the lighter dashed lines show the inclusion of molecular cooling.
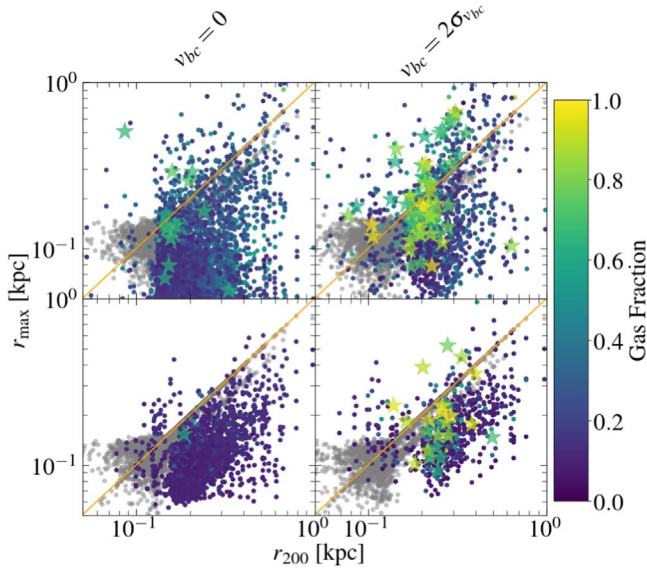
Figure 19. Scatterplot of R_{max} (v_{Rmax}) vs. the R_{200} of GP objects. The top two panels show the molecular cooling runs, and the bottom two panels show no cooling. The left column has no stream velocity and the right column is from the $v_{bc} = 2\sigma_{v_{bc}}$ runs. Stars represent SIGOs, as defined in Section 2.3. The color bar shows the gas fraction (Equation (1)). The orange line shows $R_{max} = R_{200}$. The colored points are GP objects, and the gray points are DM/G objects.
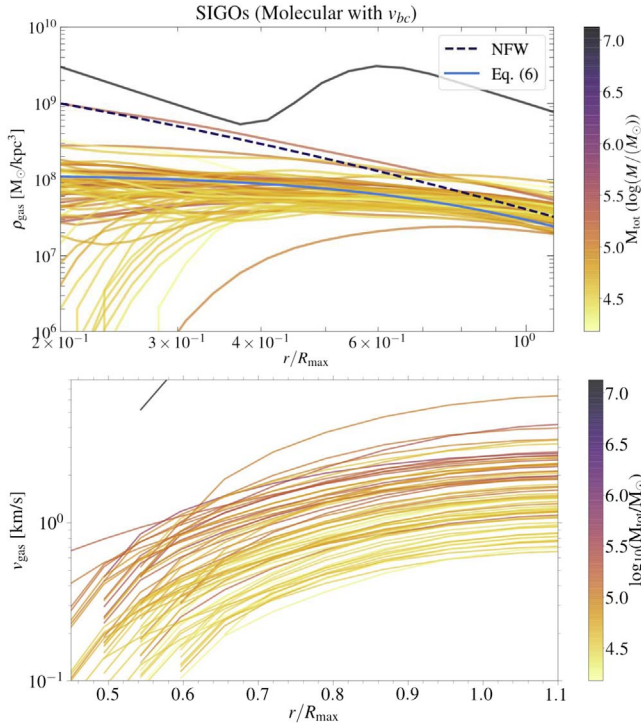

Figure 20. Top panel: density of gas in SIGOs as a function of radius, normalized to the R_{max} of the ellipsoid, for the molecular cooling run with $v_{bc} = 2\sigma_{v_{bc}}$. The density is calculated in 50 ellipsoidal shells moving out from the center of the object. The objects are colored by the mass of their gas component. An NFW profile for a $10^5 M_\odot$ halo is shown for comparison as the dashed line. Equation (6) is plotted for a SIGO with average density in solid blue. Bottom panel: rotation curves of SIGOs as a function of radius, calculated in ellipsoidal shells going outward, for the molecular cooling run with $v_{bc} = 2\sigma_{v_{bc}}$. The average velocity of the gas in an ellipsoidal shell at each radius is normalized by v_{circ}, the circular radius at the R_{max} of the ellipsoid. The objects are colored by the mass of their gas component. The average SIGO has $\bar{\rho}_{R max} = 4.14 \times 10^7 M_\odot$ kpc^{-3} and $\bar{R}_{max} = 0.240$ kpc.

R_{min}/R_{mid} for the DM component is close to one, whereas the ratio R_{mid}/R_{max} has a tail of small values. This is an indication of prolateness ($R_{min} \sim R_{mid} < R_{max}$).

In Figure 19, we plot the maximum gas ellipsoid radius against the R_{200} of its parent halo. The DM halos, in general, are much larger than the gas—this is expected. The stream velocity (as mentioned in Section 3.1.2) drives more extreme eccentricity, leading to large R_{max}.

The DM maximum ellipsoid radius is also shown as dark points in Figure 19 as a function of R_{200} found from the spherical overdensity calculation. The orange line corresponds to $R_{max,DM} = R_{200}$. In Figure 5, it was shown that low-mass objects have higher eccentricity. This is reflected in the fact that the DM distribution deviated from the 1:1 line at low masses, whereas most DM objects fall on the line at higher masses.

Finally, in Figure 20, we show the radial gas density and rotation curves of all the SIGOs from the 0vH2 run, with an NFW profile and Equation (6) overplotted. As with the low-mass DM GHOSts, the NFW profile is not a good fit. SIGOs seem to have a core, rather than a cusp.

ORCID iDs

Claire E. Williams ⓘ https://orcid.org/0000-0003-2369-2911
Smadar Naoz ⓘ https://orcid.org/0000-0002-9802-9279
William Lake ⓘ https://orcid.org/0000-0002-4227-7919
Yeou S. Chiou ⓘ https://orcid.org/0000-0003-4962-5768
Blakesley Burkhart ⓘ https://orcid.org/0000-0001-5817-5944
Federico Marinacci ⓘ https://orcid.org/0000-0003-3816-7028
Mark Vogelsberger ⓘ https://orcid.org/0000-0001-8593-7692
Gen Chiaki ⓘ https://orcid.org/0000-0001-6246-2866
Yurina Nakazato ⓘ https://orcid.org/0000-0002-0984-7713
Naoki Yoshida ⓘ https://orcid.org/0000-0001-7925-238X

References

Asaba, S., Ichiki, K., & Tashiro, H. 2016, PhRvD, 93, 023518
Barkana, R., & Loeb, A. 2001, PhR, 349, 125
Benson, A. J. 2012, NewA, 17, 175
Binney, J., & Tremaine, S. 2008, Galactic Dynamics (Princeton, NJ: Princeton Univ. Press)
Bovy, J., & Dvorkin, C. 2013, ApJ, 768, 70
Bullock, J., Kravtsov, A., & Weinberg, D. 2001, ApJ, 548, 33
Bullock, J. S., & Boylan-Kolchin, M. 2017, ARA&A, 55, 343
Bullock, J. S., Kravtsov, A. V., & Weinberg, D. H. 2000, ApJ, 539, 517
Burkert, A., Förster Schreiber, N. M., Genzel, R., et al. 2016, ApJ, 826, 214
Cadiou, C., Pontzen, A., & Peiris, H. V. 2022, MNRAS, 517, 3459
Cain, C., D'Aloisio, A., Iršič, V., McQuinn, M., & Trac, H. 2020, ApJ, 898, 168
Chiaki, G., & Wise, J. H. 2019, MNRAS, 482, 3933
Chiou, Y. S., Naoz, S., Burkhart, B., Marinacci, F., & Vogelsberger, M. 2019, ApJL, 878, L23
Chiou, Y. S., Naoz, S., Burkhart, B., Marinacci, F., & Vogelsberger, M. 2021, ApJ, 906, 25
Chiou, Y. S., Naoz, S., Marinacci, F., & Vogelsberger, M. 2018, MNRAS, 481, 3108
Danovich, M., Dekel, A., Hahn, O., Ceverino, D., & Primack, J. 2015, MNRAS, 449, 2087
Delos, M. S., & White, S. D. M. 2023, MNRAS, 518, 3509
Ebrahimian, E., & Abolhasani, A. 2022, ApJ, 926, 200
El-Badry, K., Quataert, E., Wetzel, A., et al. 2018, MNRAS, 473, 1930
Fall, S. M., & Efstathiou, G. 1980, MNRAS, 193, 189
Fialkov, A. 2014, IJMPD, 23, 1430017
Fialkov, A., Barkana, R., Tseliakhovich, D., & Hirata, C. M. 2012, MNRAS, 424, 1335
Flores, R. A., & Primack, J. R. 1994, ApJL, 427, L1
Glover, S. 2013, in Astrophysics and Space Science Library, Vol. 396, The First Galaxies, ed. T. Wiklind, B. Mobasher, & V. Bromm (Berlin: Springer), 103

Greif, T. H., White, S. D. M., Klessen, R. S., & Springel, V. 2011, ApJ, 736, 147

Guo, Q., White, S., Boylan-Kolchin, M., et al. 2011, MNRAS, 413, 101

Hegde, S., Bryan, G. L., & Genel, S. 2022, ApJ, 937, 38

Hirano, S., Hosokawa, T., Yoshida, N., & Kuiper, R. 2017, Sci, 357, 1375

Jesseit, R. 2004, PhD thesis, Ruprecht-Karls Univ. Heidelberg

Jiang, F., Dekel, A., Kneller, O., et al. 2019, MNRAS, 488, 4801

Kautsch, S. J., Grebel, E. K., Barazza, F. D., & Gallagher, J. S. 2006, A&A, 445, 765

Kneib, J.-P., & Natarajan, P. 2011, A&ARv, 19, 47

Kurapati, S., Chengalur, J. N., & Verheijen, M. A. W. 2021, MNRAS, 507, 565

Lake, W., Naoz, S., Burkhart, B., et al. 2023, ApJ, 943, 132

Lake, W., Naoz, S., Chiou, Y. S., et al. 2021, ApJ, 922, 86

Latif, M. A., Niemeyer, J. C., & Schleicher, D. R. G. 2014, MNRAS, 440, 2969

Long, H., Givans, J. J., & Hirata, C. M. 2022, MNRAS, 513, 117

Mahler, G., Natarajan, P., Jauzac, M., & Richard, J. 2023, MNRAS, 518, 54

Maller, A. H., & Dekel, A. 2002, MNRAS, 335, 487

McConnachie, A. W. 2012, AJ, 144, 4

McQuinn, M., & O'Leary, R. M. 2012, ApJ, 760, 3

Moore, B. 1994, Natur, 370, 629

Muñoz, J. B. 2019, PhRvD, 100, 063538

Nakazato, Y., Chiaki, G., Yoshida, N., et al. 2022, ApJL, 927, L12

Naoz, S., & Barkana, R. 2005, MNRAS, 362, 1047

Naoz, S., & Barkana, R. 2007, MNRAS, 377, 667

Naoz, S., Barkana, R., & Mesinger, A. 2009, MNRAS, 399, 369

Naoz, S., & Narayan, R. 2013, PhRvL, 111, 051303

Naoz, S., & Narayan, R. 2014, ApJL, 791, L8

Naoz, S., Yoshida, N., & Barkana, R. 2011, MNRAS, 416, 232

Naoz, S., Yoshida, N., & Gnedin, N. Y. 2012, ApJ, 747, 128

Naoz, S., Yoshida, N., & Gnedin, N. Y. 2013, ApJ, 763, 27

Navarro, J. F., Eke, V. R., & Frenk, C. S. 1996a, MNRAS, 283, L72

Navarro, J. F., Frenk, C. S., & White, S. D. M. 1996b, ApJ, 462, 563

Navarro, J. F., Frenk, C. S., & White, S. D. M. 1997, ApJ, 490, 493

Nguyen, T., Mishra-Sharma, S., Williams, R., & Necib, L. 2023, PhRvD, 107, 043015

O'Leary, R. M., & McQuinn, M. 2012, ApJ, 760, 4

Oman, K. A., Marasco, A., Navarro, J. F., et al. 2019, MNRAS, 482, 821

Oman, K. A., Navarro, J. F., Fattahi, A., et al. 2015, MNRAS, 452, 3650

Park, H., Ahn, K., Yoshida, N., & Hirano, S. 2020, ApJ, 900, 30

Park, H., Shapiro, P. R., Ahn, K., Yoshida, N., & Hirano, S. 2021, ApJ, 908, 96

Peebles, P. J. E. 1969, ApJ, 155, 393

Perivolaropoulos, L., & Skara, F. 2022, NewAR, 95, 101659

Popa, C., Naoz, S., Marinacci, F., & Vogelsberger, M. 2016, MNRAS, 460, 1625

Richardson, M. L. A., Scannapieco, E., & Thacker, R. J. 2013, ApJ, 771, 81

Rodriguez-Gomez, V., Genel, S., Fall, S. M., et al. 2022, MNRAS, 512, 5978

Rodriguez-Gomez, V., Sales, L. V., Genel, S., et al. 2017, MNRAS, 467, 3083

Rohr, E., Feldmann, R., Bullock, J. S., et al. 2022, MNRAS, 510, 3967

Sales, L. V., Navarro, J. F., Theuns, T., et al. 2012, MNRAS, 423, 1544

Sales, L. V., Wetzel, A., & Fattahi, A. 2022, NatAs, 6, 897

Schauer, A. T. P., Bromm, V., Boylan-Kolchin, M., Glover, S. C. O., & Klessen, R. S. 2021, ApJ, 922, 193

Schauer, A. T. P., Glover, S. C. O., & Klessen, R. S. 2017a, MmSAI, 88, 702

Schauer, A. T. P., Regan, J., Glover, S. C. O., & Klessen, R. S. 2017b, MNRAS, 471, 4878

Schaye, J., Crain, R. A., Bower, R. G., et al. 2015, MNRAS, 446, 521

Scott, D. W. 2010, WIREs Comp. Stat., 2, 497

Seljak, U., & Zaldarriaga, M. 1996, ApJ, 469, 437

Simon, J. D. 2019, ARA&A, 57, 375

Smith, B. D., Bryan, G. L., Glover, S. C. O., et al. 2017, MNRAS, 466, 2217

Somerville, R. S., & Davé, R. 2015, ARA&A, 53, 51

Somerville, R. S., Hopkins, P. F., Cox, T. J., Robertson, B. E., & Hernquist, L. 2008, MNRAS, 391, 481

Springel, V. 2005, MNRAS, 364, 1105

Springel, V. 2010, MNRAS, 401, 791

Stacy, A., Bromm, V., & Loeb, A. 2011, ApJL, 730, L1

Tanaka, T. L., & Li, M. 2014, MNRAS, 439, 1092

Tanaka, T. L., Li, M., & Haiman, Z. 2013, MNRAS, 435, 3559

Teklu, A. F., Remus, R.-S., Dolag, K., et al. 2015, ApJ, 812, 29

Tseliakhovich, D., Barkana, R., & Hirata, C. M. 2011, MNRAS, 418, 906

Tseliakhovich, D., & Hirata, C. 2010, PhRvD, 82, 083520

Uysal, B., & Hartwig, T. 2023, MNRAS, 520, 3229

Visbal, E., Barkana, R., Fialkov, A., Tseliakhovich, D., & Hirata, C. M. 2012, Natur, 487, 70

Vogelsberger, M., Genel, S., Springel, V., et al. 2014a, MNRAS, 444, 1518

Vogelsberger, M., Genel, S., Springel, V., et al. 2014b, Natur, 509, 177

Vogelsberger, M., Marinacci, F., Torrey, P., & Puchwein, E. 2020, NatRP, 2, 42

Webb, K. A., Villaume, A., Laine, S., et al. 2022, MNRAS, 516, 3318

Wechsler, R. H., & Tinker, J. L. 2018, ARA&A, 56, 435

Wheeler, C., Pace, A. B., Bullock, J. S., et al. 2017, MNRAS, 465, 2420

Yang, H., Gao, L., Frenk, C. S., et al. 2023, MNRAS, 518, 5253

Zjupa, J., & Springel, V. 2017, MNRAS, 466, 1625